Uncertainty reduction through geologically conditioned petrophysical constraints in joint inversion

Jérémie Giraud[1], Evren Pakyuz-Charrier[1], Mark Jessell[1], Mark Lindsay[1], Roland Martin[2] and Vitaliy Ogarko[1]

[1] Centre for Exploration Targeting, University of Western Australia, M006, 35 Stirling Highway, Crawley, WA 6009, Australia

[2] Géosciences Environnement Toulouse, Observatoire Midi-Pyrénées, CNRS UMR 5563, 14 Avenue Edouard Belin, 31400 Toulouse, France.

First presented at the SEG 86th Annual International Meeting.

ABSTRACT

We introduce a joint geophysical inversion workflow that aims to improve subsurface imaging and decrease uncertainty by integrating petrophysical constraints and geological data. In this framework, probabilistic geological modeling is used as a source of information to condition the petrophysical constraints spatially and to derive starting models. The workflow then utilizes petrophysical measurements to constrain the values retrieved by geophysical joint inversion. The different sources of constraints are integrated into a least-square framework to capture and integrate information related to geophysical, petrophysical and geological data. This allows us to quantify the posterior state of knowledge and to calculate posterior statistical indicators. To test this workflow, using geological field data we have generated a set of geological models, which we used to derive a probabilistic geological model. In this synthetic case study, we show that the integration of geological information and petrophysical constraints in geophysical joint inver-sion can reduce uncertainty and improve imaging. In particular, the use of petrophysical constraints retrieves sharper boundaries and better reproduces the statistics of the observed petrophysical measurements. The integration of probabilistic geological modeling permits more accurate retrieval of model geometry, and better constrains the solution

while still satisfying the statistics derived from geological data. The analysis of statistical indicators at each step of the workflow shows that 1) the inversion methodology is effective when applied to complex geology, and 2) the integration of prior information and constraints from geology and petrophysics significantly improves the inversion results while decreasing uncertainty. Lastly, the analysis of uncertainty to the integration of the conditioned petrophysical constraints also shows that, for this example, the best results are obtained for joint inversion using petrophysical constraints spatially conditioned by geological modeling.

INTRODUCTION

Over the last 15 years, significant research efforts have been directed towards the integration and use of the complementarity between different geophysical datasets in geophysical exploration to better constrain the properties of the subsurface [see Gallardo and Meju (2011), Gyulai et al. (2013) and Moorkamp et al. (2016) for more information about the different joint inversion approaches in exploration geophysics]. The main interest of joint inversion is to use and combine the strengths of different geophysical techniques to reduce the effect of non-uniqueness and uncertainty with respect to single domain inversions (Vozoff and Jupp, 1975). One of the motivations for developing these techniques is that the exploration of natural resources is becoming increasingly challenging. Hydrocarbon discoveries are becoming rarer and smaller (Crooks, 2014), and economic mineral deposit discoveries also show a decreasing trend since the mid 90's (Schodde, 2010) while deposits are found at increasing depths (Schodde, 2014). Geophysical joint inversion is one of the tools used to mitigate the risk of inaccurate interpretation of geophysical data in exploration scenarios (Rubin et al., 2006).

The usual approach to performing geophysical joint inversion is to jointly invert datasets of two or more geophysical methods using selected constraints and links between the datasets that depend on the amount and type of prior knowledge. When minimum geological information is available, several authors enforce structural constraints between the models jointly inverted (Gallardo and Meju, 2003 and 2004, Gallardo et al., 2005, Linde et al., 2006, Gallardo, 2007, Colombo and de Stefano, 2007, Fregoso and Gallardo, 2009, Hu et al. , 2009, Abubakar et al., 2012, Lelièvre et al., 2012, Bouchedda et al., 2012, Moorkamp et al., 2011 and 2013, Bennington et al., 2015, and Molodstov et al., 2013). Alternatively, when more external information is available, De Stefano et al. (2011) offer the possibility of linking multiple domains during joint inversion using either structural constraints or empirical petrophysical laws. When probabilistic geological or petrophysical data are available, several authors developed approaches involving statistical tools that account for prior information (Shamsipour et al., 2012, Reid et al., 2013, McCalman et al., 2014, Lane and Guillen, 2005, Bosch, 2004, Jardani et al., 2011, Mahardika et al., 2012, Roberts et al., 2016, Gloaguen et al., 2004). In a similar fashion, Chen et al. (2012) performs stochastic joint inversion to retrieve petrophysical properties.

In the deterministic realm, Paasche and Tronicke (2007), Sun and Li (2012, 2013) and Lelièvre et al. (2012) use clustering approaches to constrain the values of inverted properties. Garofalo et al. (2015) use a physical relationship and impose similar layer geometry during joint inversion. Another strategy has been introduced and used by Hoversten et al. (2006), Gao et al. (2012b), Giraud et al. (2013), and Liang et al. (2016) who use constitutive equations linking petrophysical properties to physical properties to retrieve petrophysical properties. Alternatively, Dell'Aversana et al. (2011 and 2016), Miotti et al. (2015), Medina et al. (2015) and Miotti and Giraud (2015) estimate petrophysical relationships using well-log data before running joint inversion to retrieve petrophysical properties (e.g., porosity, water saturation, and volume of shale).

Successful case studies have shown the relevance of integrating different geophysical datasets in complex scenarios using some of the methodologies listed above (see for example Colombo and De Stefano, 2007; Gallardo et al., 2012; De Stefano et al., 2011; Reid et al. 2013 and Medina et al., 2015). However, while geological measurements and orientation data can be used as constraints during inversion (Fullagar et al., 2008, Lelièvre and Oldenburg, 2009, and Scholl et al., 2016), less effort has been put on the quantitative integration of geostatistical modeling into geophysical joint inversion. Several studies show examples where different disciplines of geology and geophysics are integrated in a cooperative manner using expert knowledge (Jessell and Valenta, 1996, Betts et al., 2003, Lane et al., 2009, and more recently Mantovani et al., 2016 and Tschirhart et al., 2016). Quantitative integration of these two disciplines is an active, yet underexplored research area. Recent research works (Revil et al., 2015, Zhou et al., 2016, Zhang and Revil, 2015,) illustrate the increase of interest from the community, and show that integration of multiple datasets is a way forward in tackling the limitations of current inversion methodologies.

Recent advances in geostatistical modeling enable geologists to quantitatively generate more realistic geological models from surface and borehole data (Calcagno et al., 2008, Hillier et al., 2014, de la Varga and Wellmann 2016, Jessell et al., 2014). However, quantitative validation using geophysical and petrophysical data is necessary (Lindsay et al., 2013a, 2013b and 2014; Jessell et al. 2010, 2014).

To mitigate the lack of quantitative integration between geology and geophysics, several authors developed geophysical inversion algorithms addressing the geometry of the inverted models. Fullagar and Pears (2007), Gallardo et al. (2005), Guillen et al. (2008), Wellmann et al. (2013) and Zhang and Revil (2015) developed geology-geophysics inversion algorithms that allow the geometry of the geological structures to vary in order to honour geophysical data. Li et al. (2010), Davis et al. (2012), McMillan et al. (2015) and Balidemaj and Remis (2010) parameterize geology to include model geometry in inversion. To cope with the additional variables introduced by geological modeling, Doetsch et al. (2010) allow their algorithm to discretize the medium in layers. Similarly, Juhojuntti and Kamm (2015) introduce a layered joint inversion scheme. These layered schemes attempt to solve hydrogeological problems, and the investigated models do not have the same geological complexity encountered in hard rock scenarios. With this regard, Lelièvre et al. (2012, 2015) developed a more general method using a stochastic approach to invert for contact surface geometry.

In joint inversion, the hypotheses underlying structure-based approaches (e.g. the curvature of the models as introduced by Haber and Oldenburg, 1997, or the cross-product of the gradients of the model as introduced by Gallardo and Meju, 2003), may exert little influence on the inversion depending on the geological setting of the area, in cases where gradients of the considered properties are not parallel. A possible strategy to complement joint inversion approaches relying on structural similarities is to link the different geophysical methods through constraints derived from non-geophysical field measurements. In this work, we propose such a methodology which we apply to a general case where some of the assumptions commonly made to link models in joint inversion are not valid across the entire model.

As discussed above, the use of petrophysical laws can be used to link different domains in joint inversion and to avoid making hypotheses on the structural setting of the medium. However, accurate determination and upscaling of these laws to the entire model is challenging and sufficient prior information is necessary to determine and tune them. On the other hand, statistical petrophysical analysis is a powerful tool to derive correlations between physical properties. In addition to the templates using mechanical properties, petrophysical templates have been produced to classify rocks according to their mineral content or lithology using, among others, density and magnetic susceptibility. Some authors (Barlow 2004, Hatfield et al. 2002, Rao 2008) also use plots of density and magnetic susceptibility to discriminate lithologies, although in hard rock scenarios lithological classes may overlap (Williams, 2009). In this article, we use the statistics of the petrophysical properties in cross-plot domain and link it to lithology from probabilistic geological modeling to constrain inversion. We address the petrophysical constraints in the same spirit as the clustering approaches introduced by Sun and Li (2012, 2013 and 2016) and Lelièvre et al. (2012). The clustering approach has been further investigated by Carter-McAuslan et al. (2015), applied to field data by Sun and Li (2015 and 2017b), and extended, for single domain inversion, to the use of geological interpretation by and Rapstine et al. (2016). We adapt and extend these concepts to a joint least-square inversion framework, in which we integrate probabilistic geological information.

Inverse problems in geosciences typically have a high dimensionality and are under-constrained (Li and Oldenburg, 1998, and McCalman et al., 2014). The workflow we present integrates complementary sources of information to constrain geophysical inversion in order to reduce both uncertainty and non-uniqueness due to the effect of the ill-posedness of the inverse problem. Geological prior information is commonly used to mitigate non-uniqueness and as a means to derive starting and reference models. However, the reliability of geological prior information is linked to the level of the geologist's expertise, and is therefore affected by biases (Bond et al., 2007, and Bond, 2015). To alleviate this, we introduce a methodology that integrates probabilistic geological modeling, petrophysical measurements and geophysical joint inversion in a fully integrated workflow. In this way, our methodology accounts quantitatively for prior uncertainty relating to geology, petrophysics and geophysics. We obtain *spatially conditioned petrophysical constraints* by combining surface petrophysical measurement and the geological model resulting from what we refer to as Monte Carlo Uncertainty Estimation (MCUE).The novelty of the work presented in this article is that not only do we take advantage of complementary geophysical methods in joint inversion, we also combine probabilistic geological modeling and petrophysical measurements to derive constraints for inversion. We use this to integrate the statistics of the petrophysical measurements, geological modeling and geophysical data. This allows us to calculate posterior uncertainty indicators and to evaluate the quality of the results.

In this manuscript we first introduce the theoretical background describing the methodology we have used, detailing the inversion algorithm and how geological modeling and petrophysical constraints are derived and integrated. Then, prior to introducing the synthetic case study we generated to test our workflow we explain our choice of statistical tools for uncertainty analysis. The final section of the paper analyzes the results using the selected statistical tools. This section shows the improvements and limitations of the integration of geological modeling and petrophysical constraints in geophysical inversion.

METHODOLOGY

To integrate geological measurement in the inversion we use a probabilistic geological modeling approach accounting for geological uncertainty. We use what we refer to *Monte Carlo Uncertainty Estimator* (MCUE). It utilizes stochastic modeling to obtain a probabilistic geological model (i.e. a lithology probability for each voxel in the model). MCUE is based on a Monte Carlo perturbation of geological input data used to produce a relatively large number of possible geological models (typically between several hundred to a few thousand), which we couple with the statistics of the petrophysical measurements to constrain the inversions (joint and single domain). MCUE builds upon the work of Wellmann et al. (2010), Jessell et al. (2010), Lindsay et al. (2012), and Pakyuz-Charrier et al. (2015). As a statistical description of a wide range of possible geological models, MCUE removes the need for a best guess model.

The workflow we present here can be divided into several steps. The first two steps of the workflow are to perform MCUE analysis and in parallel derive statistical laws that reproduce the statistics of petrophysical measurements (see subsection on petrophysical constraints, equation (6)). The next step consists of combining the geological statistical model with the former statistical laws to obtain starting models and constraints for inversion. Then, geophysical inversions are performed. After joint inversion, the last step of the workflow is the calculation of uncertainty indicators. This allows us to quantify the reduction of uncertainty, to evaluate the effect of integrating geology and petrophysics in single domain and joint inversion. Zones of higher uncertainty, which remain poorly constrained, can be identified as the foci for further study (Lindsay et al., 2012, Wellman et al., 2010).

The test data set uses a geological model computed from actual surface structural measurements (rock type, foliations, dip and strike and surface contact geometry) but for which we increased the complexity by adding additional structures in order to test the robustness of the methodology. We use GeoModeller 3.3 to generate models. This relatively complex synthetic case study allows us to evaluate the behaviour of the inversion algorithm in real cases studies, where there is no control on the actual model. To test and illustrate the workflow we simulate gravity and magnetic surface data.

Workflow summary

The workflow is summarised in Figure 1. Before inversion, the first step is to translate prior geological and petrophysical data into information that can be used during the inversion. In the MCUE approach, geological modeling uses geological data to produce a probabilistic geological model. A mixture model that reproduces the statistics of the petrophysical measurements is derived. The probabilistic geological model and the mixture model are used to derive starting models, global (spatially invariant) and geologically conditioned petrophysical constraints. Once these are available, constrained single domain inversions are performed first. These are used as controls to assess the improvement brought by constraints and to compare with joint inversion. The next step of the workflow is to run joint inversion. After joint inversions have been performed, the last step of the workflow is the estimation of posterior uncertainty using uncertainty indicators for the inverted models.

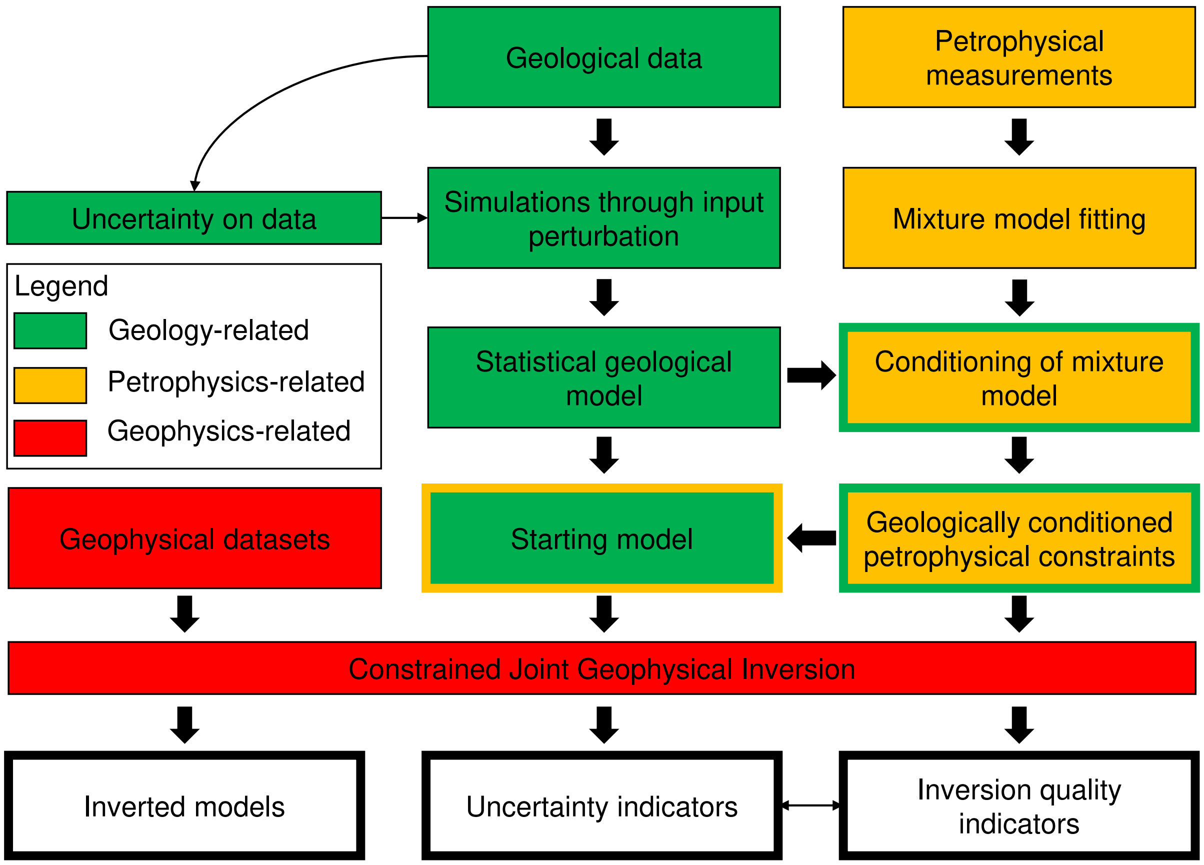

Figure 1. Integrated joint inversion workflow summary illustrating the interaction between geology, petrophysics and geophysics.

Inversion framework

Objective function

We formulate the inverse problem in a least-square sense as detailed in Tarantola (2005).

We derive the following objective function (equation 1):

$$\theta(\boldsymbol{m}) = \left(\boldsymbol{d} - \boldsymbol{g}(\boldsymbol{m})\right)^T \boldsymbol{C}_{\boldsymbol{d}}^{-\boldsymbol{1}}\left(\boldsymbol{d} - \boldsymbol{g}(\boldsymbol{m})\right) + \left(\boldsymbol{m} - \boldsymbol{m}_{\boldsymbol{p}}\right)^T \boldsymbol{C}_{\boldsymbol{m}}^{-\boldsymbol{1}} \left(\boldsymbol{m} - \boldsymbol{m}_{\boldsymbol{p}}\right)$$
$$+ \delta^G(\boldsymbol{p}_{\boldsymbol{max}} - \boldsymbol{p}(\boldsymbol{m}))^T \boldsymbol{C}_{\boldsymbol{p}}^{\boldsymbol{G}^{-\boldsymbol{1}}}(\boldsymbol{p}_{\boldsymbol{max}} - \boldsymbol{p}(\boldsymbol{m})) \tag{1}$$
$$+ \delta^M(\boldsymbol{p}_{\boldsymbol{max}} - \boldsymbol{p}(\boldsymbol{m}))^T \boldsymbol{C}_{\boldsymbol{p}}^{\boldsymbol{M}^{-\boldsymbol{1}}}(\boldsymbol{p}_{\boldsymbol{max}} - \boldsymbol{p}(\boldsymbol{m}))$$

where

$$\boldsymbol{g}(\boldsymbol{m}) = \begin{bmatrix} \boldsymbol{g}_{\boldsymbol{G}}(\boldsymbol{m}) \\ \boldsymbol{g}_{\boldsymbol{M}}(\boldsymbol{m}) \end{bmatrix}, \boldsymbol{m} = \begin{bmatrix} \boldsymbol{m}^{\boldsymbol{G}} \\ \boldsymbol{m}^{\boldsymbol{M}} \end{bmatrix}, \boldsymbol{d} = \begin{bmatrix} \boldsymbol{d}_{\boldsymbol{G}} \\ \boldsymbol{d}_{\boldsymbol{M}} \end{bmatrix}, \boldsymbol{C}_{\boldsymbol{d}} = \begin{bmatrix} \boldsymbol{C}_{\boldsymbol{d}}^{\boldsymbol{G}} & \boldsymbol{0} \\ \boldsymbol{0} & \boldsymbol{C}_{\boldsymbol{d}}^{\boldsymbol{M}} \end{bmatrix}, \boldsymbol{C}_{\boldsymbol{m}} = \begin{bmatrix} \boldsymbol{C}_{\boldsymbol{m}}^{\boldsymbol{G}} & \boldsymbol{0} \\ \boldsymbol{0} & \boldsymbol{C}_{\boldsymbol{m}}^{\boldsymbol{M}} \end{bmatrix} \tag{2}$$

In the equations above $\boldsymbol{m}$ represents the model of inverted properties while $\boldsymbol{d}$ represents the geophysical measurements to be inverted. $\boldsymbol{g}$ is the forward operator that calculates the data model $\boldsymbol{m}$ produces. $\boldsymbol{m}_{\boldsymbol{p}}$ is the prior model, which we also use as starting model. $\boldsymbol{C}_{\boldsymbol{m}}$ and $\boldsymbol{C}_{\boldsymbol{d}}$ are spherical covariance matrices corresponding to model and data noise, respectively. G and M superscripts and subscripts refer to gravity and magnetics, respectively.

$\boldsymbol{C}_{\boldsymbol{p}}$ is what we call the petrophysical probability covariance matrix (described later). $\boldsymbol{p}$ is the probability density function derived from petrophysical measurements, calculating the likelihood of model $\boldsymbol{m}$, $\boldsymbol{p}(\boldsymbol{m})$, of a given model $\boldsymbol{m}$. $\boldsymbol{p}_{\boldsymbol{max}}$ is the mode of $\boldsymbol{p}(\boldsymbol{m})$. Superscript T denotes the transpose operator. δ^G and δ^M are scalars that are set either to 0 or 1 depending on the type of inversion.

In the objective function, the first two terms in equation (1) relate to data and model misfit, respectively. The third and fourth terms are specific to petrophysical constraints on gravity and magnetic data inversion, respectively. They relate to the probabilistic description of the model based on independent, non-geophysical sources of information. $\boldsymbol{p}$ encapsulates the coupling in joint inversion. It is a function of both $\boldsymbol{m^G}$ and $\boldsymbol{m^M}$ and is defined such that p : $N \times N \rightarrow N$ with $\boldsymbol{m}$ as input, returning the corresponding $\boldsymbol{p}(\boldsymbol{m})$ values.

Optimization scheme

We minimize the joint objective function $\theta(\boldsymbol{m})$ (equation 1) using a Newton least-squares algorithm, adapting the solution proposed by Tarantola (1984) to our joint inversion problem. The model is iteratively updated using a fixed-point method as follows (equation 3) for gravity data and magnetic data:

$$\begin{aligned}
\boldsymbol{m}_{\boldsymbol{k+1}}^{\boldsymbol{G}} &= \boldsymbol{m}_{\boldsymbol{k}}^{\boldsymbol{G}} + \left[\boldsymbol{A}_k^{\boldsymbol{G}^T} \boldsymbol{C}_{\boldsymbol{d}}^{\boldsymbol{G}^{-1}} \boldsymbol{A}_k^{\boldsymbol{G}} + \boldsymbol{C}_{\boldsymbol{m}}^{-1} + \boldsymbol{J}_k^{\boldsymbol{G}^T} \boldsymbol{C}_{\boldsymbol{p}}^{\boldsymbol{G}^{-1}} \boldsymbol{J}_k^{\boldsymbol{G}}\right]^{-1} \left[\boldsymbol{A}_k^{\boldsymbol{G}^T} \boldsymbol{C}_{\boldsymbol{d}}^{\boldsymbol{G}^{-1}} \left(\boldsymbol{d}_{\boldsymbol{G}} - \boldsymbol{g}_G\left(\boldsymbol{m}_{\boldsymbol{k}}^{\boldsymbol{G}}\right)\right)\right. \\
&\qquad \left. - \boldsymbol{C}_{\boldsymbol{m}}^{\boldsymbol{G}^{-1}}\left(\boldsymbol{m}_{\boldsymbol{k}}^{\boldsymbol{G}} - \boldsymbol{m}_{\boldsymbol{p}}^{\boldsymbol{G}}\right) + \boldsymbol{J}_k^{\boldsymbol{G}^T} \boldsymbol{C}_{\boldsymbol{p}}^{\boldsymbol{G}^{-1}}\left(\boldsymbol{p}_{\boldsymbol{max}} - \boldsymbol{p}(\boldsymbol{m}_k)\right)\right], and \\
\boldsymbol{m}_{\boldsymbol{k+1}}^{\boldsymbol{M}} &= \boldsymbol{m}_{\boldsymbol{k}}^{\boldsymbol{M}} + \left[\boldsymbol{A}_k^{\boldsymbol{M}^T} \boldsymbol{C}_{\boldsymbol{d}}^{\boldsymbol{M}^{-1}} \boldsymbol{A}_k^{\boldsymbol{M}} + \boldsymbol{C}_{\boldsymbol{m}}^{-1} + \boldsymbol{J}_k^{\boldsymbol{M}^T} \boldsymbol{C}_{\boldsymbol{p}}^{\boldsymbol{M}^{-1}} \boldsymbol{J}_k^{\boldsymbol{M}}\right]^{-1} \left[\boldsymbol{A}_k^{\boldsymbol{M}^T} \boldsymbol{C}_{\boldsymbol{d}}^{\boldsymbol{M}^{-1}} \left(\boldsymbol{d}_{\boldsymbol{M}}\right.\right. \\
&\qquad \left.\left. - \boldsymbol{g}_{\boldsymbol{M}}\left(\boldsymbol{m}_{\boldsymbol{k}}^{\boldsymbol{M}}\right)\right) - \boldsymbol{C}_{\boldsymbol{m}}^{\boldsymbol{M}^{-1}}\left(\boldsymbol{m}_{\boldsymbol{k}}^{\boldsymbol{M}} - \boldsymbol{m}_{\boldsymbol{p}}^{\boldsymbol{M}}\right) + \boldsymbol{J}_k^{\boldsymbol{M}^T} \boldsymbol{C}_{\boldsymbol{p}}^{\boldsymbol{M}^{-1}}\left(\boldsymbol{p}_{\boldsymbol{max}} - \boldsymbol{p}(\boldsymbol{m}_k)\right)\right],
\end{aligned} \tag{3}$$

with

$$\begin{cases}
\boldsymbol{A}_k = \begin{bmatrix} \boldsymbol{A}_k^{\boldsymbol{G}} \\ \boldsymbol{A}_k^{\boldsymbol{M}} \end{bmatrix} = \begin{bmatrix} \boldsymbol{A}_{k=0}^{\boldsymbol{G}} \\ \boldsymbol{A}_{k=0}^{\boldsymbol{M}} \end{bmatrix} = \begin{bmatrix} \dfrac{\partial \boldsymbol{g}_{\boldsymbol{G}}(\boldsymbol{m}_{\boldsymbol{G}})}{\partial \boldsymbol{m}_{\boldsymbol{G}}}, \dfrac{\partial \boldsymbol{g}_{\boldsymbol{M}}(\boldsymbol{m}_{\boldsymbol{M}})}{\partial \boldsymbol{m}_{\boldsymbol{M}}} \end{bmatrix}^T \\
\boldsymbol{J}_k = \begin{bmatrix} \boldsymbol{J}_k^{\boldsymbol{G}}(\boldsymbol{m}_k) \\ \boldsymbol{J}_k^{\boldsymbol{M}}(\boldsymbol{m}_k) \end{bmatrix} = \begin{bmatrix} \dfrac{\partial \boldsymbol{p}(\boldsymbol{m}_k)}{\partial \boldsymbol{m}_{\boldsymbol{G}}}, \dfrac{\partial \boldsymbol{p}(\boldsymbol{m}_k)}{\partial \boldsymbol{m}_{\boldsymbol{M}}} \end{bmatrix}^T
\end{cases} \tag{4}$$

where $\boldsymbol{A}_k$ and $\boldsymbol{J}_k$ are, respectively, the matrices of the partial derivatives of $\boldsymbol{g}$ and $\boldsymbol{p}$ with respect to $\boldsymbol{m}$. Subscript k denotes the k-th iteration. The inverse of the Hessian matrix (the left part of the second term in equation 3) is calculated using a Cholesky direct solver based on Gauss pivot rules. Partial derivative matrices $\boldsymbol{A}_k$ are calculated analytically while the elements of $\boldsymbol{J}_k$ are calculated using first order finite difference derivatives.

Stopping criteria

The number of iterations is controlled by two criteria: iterations stop when the model updates stabilize below a chosen threshold; or when the Bravais-Pearson correlation (BP, also called linear correlation) between the inverted models and the BP correlation between the magnitudes of the spatial gradients of inverted models have both reached a plateau. We calculate the BP correlation as follows (equation 5):

$$r\left(\boldsymbol{T}^{(1)},\boldsymbol{T}^{(2)}\right) = \frac{\overline{\boldsymbol{T}^{(1)}\,\boldsymbol{T}^{(2)}} - \overline{\boldsymbol{T}^{(1)}}\ \overline{\boldsymbol{T}^{(2)}}}{\left\{\left(\overline{{\boldsymbol{T}^{(1)}}^2} - \overline{\boldsymbol{T}^{(1)}}^2\right)\left(\overline{{\boldsymbol{T}^{(2)}}^2} - \overline{\boldsymbol{T}^{(2)}}^2\right)\right\}^{1/2}} = \frac{\left(\boldsymbol{T}^{(1)} - \overline{\boldsymbol{T}^{(1)}}\right)\cdot\left(\boldsymbol{T}^{(2)} - \overline{\boldsymbol{T}^{(2)}}\right)}{\left\|\boldsymbol{T}^{(1)} - \overline{\boldsymbol{T}^{(1)}}\right\|\left\|\boldsymbol{T}^{(2)} - \overline{\boldsymbol{T}^{(2)}}\right\|}, \tag{5}$$

where $\boldsymbol{T}^{(1)}$ and $\boldsymbol{T}^{(2)}$ are the properties for which the correlation is calculated, and the horizontal bar operator is the arithmetic average operator. We calculate r for $\boldsymbol{T}^{(1)}$ and $\boldsymbol{T}^{(2)}$ being the inverted models or the magnitude of their gradients. In the second case, $\boldsymbol{T}^{(1)}$ and $\boldsymbol{T}^{(2)}$ are calculated as $\boldsymbol{T}^{(1)} = \left|\nabla \boldsymbol{m}^{(1)}\right|$, $\boldsymbol{T}^{(2)} = \left|\nabla \boldsymbol{m}^{(2)}\right|$ for a given set of models. r can be interpreted as the cosine similarity between the vectors $\boldsymbol{T}^{(1)} - \overline{\boldsymbol{T}^{(1)}}$ and $\boldsymbol{T}^{(2)} - \overline{\boldsymbol{T}^{(2)}}$, $\cos\left(\boldsymbol{T}^{(1)} - \overline{\boldsymbol{T}^{(1)}}, \boldsymbol{T}^{(2)} - \overline{\boldsymbol{T}^{(2)}}\right)$. It reaches its maximum value when the two vectors have the same orientation in the entirety of the model. Therefore, we can use $r\left(\left|\nabla \boldsymbol{m}^{(1)}\right|, \left|\nabla \boldsymbol{m}^{(2)}\right|\right)$ to characterize the geometrical convergence of the inverted models during inversion. Similarly, $r\left(\boldsymbol{m}^{(1)}, \boldsymbol{m}^{(2)}\right)$ provides a metric characterizing the degree of linear relationship between the two models during inversion. When r reaches a plateau, the changes in the models are not sufficient to have an impact on r, meaning that, with regards to geometrical considerations, inversion has converged.

Geological modeling

Building geological models from geological observations depends on the interpreter (Bond et al. 2007), on the type of data (Bond, 2015) and of the quality of the data and how well it represent nature (Alcade et al., 2017). Under these conditions, rigorous prior uncertainty estimation on geological prior models is difficult to obtain even with error estimates on input data. Thus, following the method described by Wellmann and Regenauer-Leib (2012), Lindsay et al. (2012, 2013) and Jessell et al. (2014), we use a geological modeling scheme capable of generating a 'suite' of geological models, which allows the quantification of uncertainty inherent in a 3D model.

Geological models are drawn from probability distributions defined by basic assumptions about the statistics of the errors on geological data using a Monte-Carlo simulation. In MCUE, topological rules prevent unstructured behavior, ensuring that the models are geologically plausible. The data replacement and perturbation procedure used in the Monte Carlo simulation is an extension of work by Wellmann et al (2010), Jessell et al. (2010) and Lindsay et al. (2012) using ideas of Pakyuz-Charrier et al. (2015).

The probability of presence of a lithology is calculated for each cell of the model. For the $\boldsymbol{i}$-th cell of the medium, the probability of presence of rock unit $\boldsymbol{k}$ is $\boldsymbol{\psi_{k,i}}$. That is, the end product of MCUE is analogous to a 'geological model with an uncertainty estimate'. In the workflow we present in the paper, the results from of MCUE are used to calculate several terms in equation (1): $\boldsymbol{p(m)}, \boldsymbol{p_{max}}$.

Petrophysical constraints

The petrophysical constraints are applied to inversion through the minimization of the third term of equation (1) simultaneously to the minimization of the data and model misfit terms. To maximize the similarity between the statistical properties of the measured petrophysical data and the inverted model we follow concepts introduced by Sun and Li (2012, 2013) and Lelièvre et al. (2012). We assume that the petrophysical properties are normally distributed for each rock type. Therefore, there exists a statistical model that can represent the probability distribution of the overall measurements. $\boldsymbol{p}(\mathbf{m})$ is formulated using a mixture model as (equation 6):

$$\boldsymbol{p}(\boldsymbol{m}) = \sum_{k=1}^{n_f} \omega_k \mathrm{N}(\boldsymbol{m}|\boldsymbol{\mu_k}, \boldsymbol{\sigma_k}) \tag{6}$$

In equation (6), n_f is the number of lithologies observed in the petrophysical measurements. The parameters of $\mathrm{N}(\boldsymbol{m}|\boldsymbol{\mu_k}, \boldsymbol{\sigma_k})$, $\boldsymbol{\sigma_k}$ and $\boldsymbol{\mu_k}$, are estimated using an expectation maximization algorithm. Although there are no constraints on the type of distribution to be used, we assume, to fix ideas, a normal distribution N. As described in Grana and Della Rossa (2010) and Grana et al. (2017), Gaussian mixture models can be used in statistical of rock physics modelling. In equation (6), each distribution is characterized by a mean value vector, $\boldsymbol{\mu_k}$, which corresponds to the clusters' centers, and the associated covariance matrix, $\boldsymbol{\sigma_k}$. ω_k is the relative weight of the k-th lithology in the measurements. $\boldsymbol{\mu_k}$, $\boldsymbol{\sigma_k}$ and ω_k are obtained by fitting equation (6) to the petrophysical measurements. The correlation between petrophysical properties of different nature (for example density and magnetic susceptibility) is captured in the off-diagonal elements of $\boldsymbol{\sigma_k}$, which is a full matrix.

After the mixture is characterized we calculate the diagonal matrix $\boldsymbol{C_p}$ as follows:

$$\boldsymbol{C_p} = \left(\max_{k=1:n_f} diag(\boldsymbol{\sigma_k}) \right)^{-1} \boldsymbol{I}, \tag{7}$$

This method of weighting is chosen to enhance the contribution of well-defined components of the mixture model in the model update.

Model covariance matrix $\boldsymbol{C_m}$ is preconditioned through the application of a depth-weighting inverse power law function following Li and Oldenburg (1998) and Li and Chouteau (1999) for gravity, and following Li and Oldenburg (1996) for magnetic data, to balance decreasing sensitivity with depth. For the conditioning of petrophysical constraints by geological modeling, $\boldsymbol{p(m)}$ is calculated using both the results from MCUE and the mixture estimated in equation (6). The probability of presence of the different rock units $\psi_{k,i}$, in each cell of the medium, is accounted for. In such case, $\boldsymbol{p(m)}$ is calculated as follows (equation 8):

$$\boldsymbol{p}(\boldsymbol{m}) = \begin{bmatrix} p_1(m_1) \\ p_2(m_2) \\ \dots \\ p_{n_m}(m_{n_m}) \end{bmatrix}, \text{where: } p_i(m_i) = \sum_{k=1}^{n_f} \psi_{k,i}\, \mathbf{N}(m_i | \boldsymbol{\mu_k}, \boldsymbol{\sigma_k}), \tag{8}$$

where n_m is the total number of cells of the model. The conditioning of the petrophysical constraints is illustrated as follows (Figure 2):

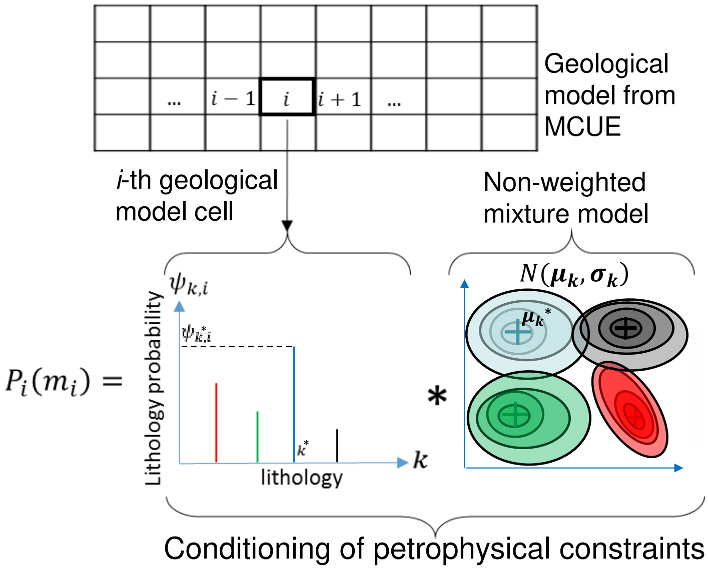

Figure 2. Principle of conditioning of petrophysical constraints by EG.

After conditioning of $\boldsymbol{p}(\boldsymbol{m})$ (equation 6 and 8) the term $\boldsymbol{p_{max}}$ (in equation 1 and 3) can be calculated. It is calculated as follows (equation 9), for the i-th cell of the medium:

$$\begin{cases} k^* = \left\{ k | \psi_{k,i} = \max_{n=1:n_f} \psi_{n,i} \right\} \\ p_{max_i} = \psi_{k^*,i} \sum_{j=1}^{n_f} \mathbf{N}\left(\mu_{k^*} | \boldsymbol{\mu_j}, \boldsymbol{\sigma_j}\right) \end{cases} \tag{9}$$

MCUE is also used to calculate starting models for inversions using conditioned petrophysics. In such case, the starting model is determined by calculating the mathematical expectation of $\boldsymbol{p}(\boldsymbol{m})$ after it is conditioned by geological modeling. The use of the mathematical expectation is convenient here because it represents the average model obtained after a sufficiently large number of draws using Monte Carlo sampling in model space, which is performed during MCUE. The starting model is calculated as follows for the i-th cell (equation 10):

$$m_{0,i} = \sum_{k=1}^{n_f} \psi_{k,i}\, \mu_k \tag{10}$$

In the case of global petrophysical constraints, $\boldsymbol{p}(\boldsymbol{m})$ is calculated assuming equiprobability for all lithologies (all $\psi_{k,i}$ being equal to $\frac{1}{n_f}$), and $m_0 = 0$.

Uncertainty analysis and inversion uncertainty indicators

In our workflow, we monitor inversion and perform posterior statistical analysis that incorporates geological and petrophysical information: we study the convergence, reduction of non-uniqueness and increase of model likelihood. To this end, we calculate the petrophysical likelihood of the inverted model and indicators it allows us to derive. In addition, the posterior analysis of the correlations introduced in the previous subsection provides information on the degree of coupling between the inverted models. For tests on synthetic models, we calculate the root-mean-square (RMS) model misfits. For geophysical (field or synthetic) data we calculate the first term in equation (1), corresponding to the data misfit term,

The petrophysical likelihood function of the inverted models is calculated a posteriori for each cell of the medium, using geologically conditioned petrophysical constraints (equation 8):

$$\boldsymbol{L} = \boldsymbol{p}(\boldsymbol{m_f})\,, \tag{11}$$

where $\boldsymbol{p}$ is conditioned by MCUE (as in equation (8)) and $\boldsymbol{m_f}$ is the model obtained after convergence of the algorithm.

In the definition of the petrophysical likelihood $\boldsymbol{L}$ (equation 11) we do not include the term related to geophysical data fit in order to isolate the reduction of geological and petrophysical uncertainty brought by geophysical inversion.

As stated above, $\boldsymbol{L}$ is used to derive other indicators. It is straightforward to show that, assuming that the observables are constituted of the parameters defining $\boldsymbol{p}$ in equation (8) and that the unknown parameter is the model, we can derive a result analogous to the Fisher information (introduced by Fisher, 1925; see Kitanidis, 1995, Snodgradd and Kitanidis, 1997, who use the Fisher information matrix in their inversion scheme) in petrophysical domain, which estimates how much curvature (under-determination) exists around the petrophysical likelihood value. In the present case, it provides an indicator as to the sharpness of $\boldsymbol{L}$ in the neighbourhood of the obtained solutions. Essentially, Fisher information quantifies how stable **L** is where it is estimated. This, in turn, allows for a better understanding of uncertainty because it evacuates the common ambiguities as compared to moment generating functions (such as about the mean, variance, skew, etc). Let this indicator be expressed as follows:

$$\begin{aligned} \boldsymbol{I_F} &= [I_F^G, I_F^M] = \left[\mathbb{E}\left\{\left(S_i^G\right)^2_{i=1,..,n_m}\right\}, \mathbb{E}\left\{(S_i^M)^2_{i=1,..,n_m}\right\}\right] \\ &= \left[var\left(S^G_{i=1,..,n_m}\right),\ var\left(S^M_{i=1,..,n_m}\right)\right], \end{aligned} \tag{12}$$

with

$$S_i^G = \frac{J^G_{f,ii}}{L_i}, S_i^M = \frac{J^M_{f,ii}}{L_i}, \tag{13}$$

where $\mathbb{E}$ is the mathematical expectation operator, var symbolizes the variance (square of standard deviation), and $\boldsymbol{J_f}$ represents the Jacobian matrix (equation 4) of the petrophysical constraints for $\boldsymbol{m} = \boldsymbol{m_f}$. The first and second element of $\boldsymbol{I_F}$ refer to the density contrast and magnetic susceptibility models, respectively. S, called the score, is obtained by calculating the partial derivative of the logarithm of the likelihood function with respect to the model parameters. We assume that the values are centered on the cluster centers. In such case, the expected value, or mean, of S is zero (e.g., points are evenly distributed around the cluster centers). Fisher's information becomes the variance of the score, and indicates how stable the solution is with respect to the parameters. Therefore, ideally, for the Gaussian mixture model we use, it is flat in the neighborhood of the cluster centers and sharper farther away up until a few standard deviations, each term of equation (12) would decrease and tend towards 0when an optimal model maximizing $\boldsymbol{L}$ is obtained. To characterize the degree of uncertainty of the result we calculate another indicator, consisting in the average normalized RMS of the score of the inverted models. It is expressed as follows:

$$S_{rms} = \frac{1}{2}\left\{\frac{1}{\max\limits_{j=1:n_m} S_j^G}\sqrt{\frac{1}{n_m}\sum\nolimits_{i=1}^{n_m}\left(S_i^G\right)^2} + \frac{1}{\max\limits_{j=1:n_m} S_j^M}\sqrt{\frac{1}{n_m}\sum\nolimits_{i=1}^{n_m}(S_i^M)^2}\right\} \tag{14}$$

It calculates the sum of the normalized RMS of the score for density contrast and magnetic susceptibility. Similarly to $\boldsymbol{I_F}$, S_{rms} would be equal to zero for a perfectly constrained model. Final values for the different inversions and analysis of the value of $\boldsymbol{L}$, $\boldsymbol{I_F}$ and S_{rms} allow us to estimate the amount of information from the petrophysical constraints that contributed to the inversion. These indicators also show how well the algorithm converged, and permit to estimate the reduction of uncertainty.

SYNTHETIC GEOPHYSICS WITH REAL GEOLOGY

Geological context and modeling

We generated a 3D geological model derived from surface data from the Mansfield area (Victoria, Australia). The original model is the Mansfield sedimentary basin located North-West to Mansfield, Victoria, Australia. It presents itself as a Carboniferous mudstone and sandstone syncline oriented N170. It abuts a faulted contact with a Silurian-Devonian folded sandstone basement to the South West. After we obtained a geological model that reproduces field geological data we increased the complexity of the model to better test the inversion algorithm by the addition of a fictitious North-South fault across the Carboniferous basin and of an imaginary mafic intrusion to the South West corner of the model, in the Devonian basement; details on the original model can be found in *GeoModeller User Manual, Tutorial case study H (Mansfield)*. The reference geological model was constructed without addressing errors in geological data (e.g. using unperturbed input data), and is shown on Figure 3. The map view shows that the model contains faults that intersect. Cross-section A-B was chosen for the testing the geophysical part of the workflow as it shows complex, realistic structures that can be challenging to retrieve through inversion. Since we are only solving a 2D problem, the obliquity of the section to the regional structures does not pose a problem.

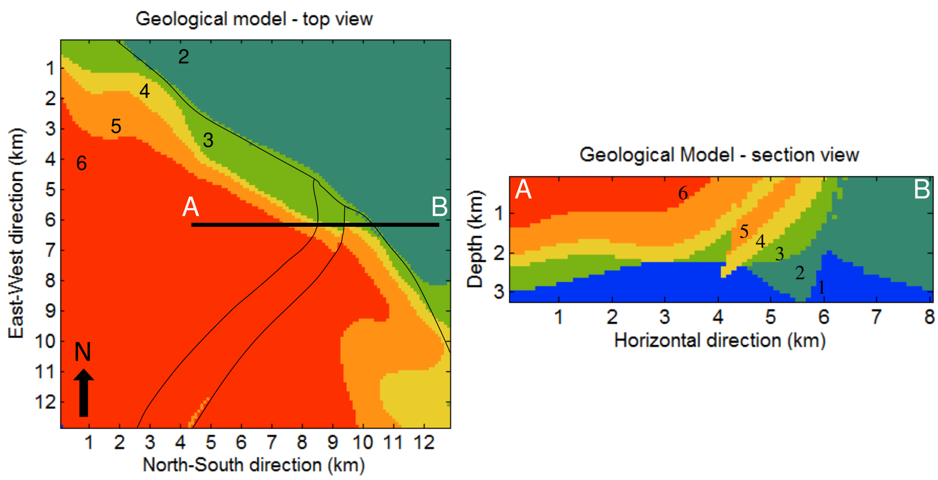

Figure 3. Reference geological model used for geological modeling. Faults are shown by black lines in map view. The left part shows the map view while the right hand part shows the

extracted cross-section A-B, which has been extracted from this volume and is used as the reference geological model. The numbers on the Figure indicate the index assigned to the lithologies.

We applied the MCUE method to the geological reference model by assuming that errors on orientation data can be modelled using the von Mises-Fisher distribution, using a solid angle of approximately 0.1 steradians. This corresponds to the case scenario where 99% of the orientation data lies within a 22 degree aperture cone. 300 samples generated by the Monte-Carlo simulation in MCUE allowed us to obtain a stable 3D statistical model, shown in Figure 4 for cross-section A-B.

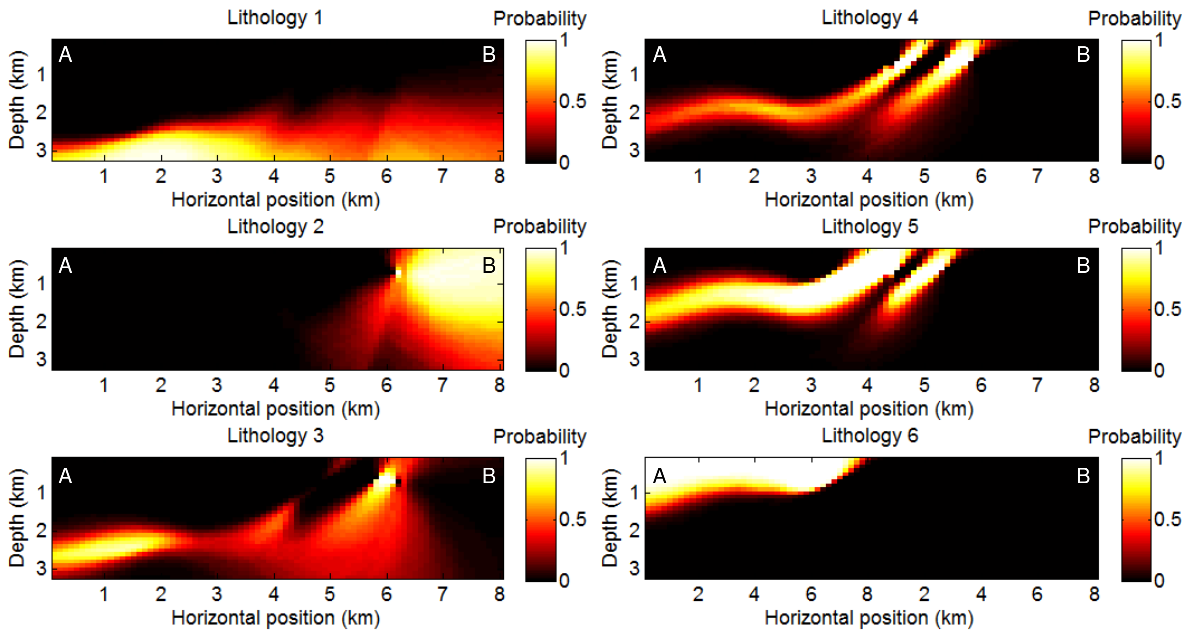

Figure 4. Probability of presence for the different lithologies for cross-section A-B. These probabilities have been obtained from MCUE on the whole geological model and extracted along the cross-section to be used in a 2D setting.

Figure 4 shows the resulting probability of the presence at a given location of each of the modelled lithologies after applying MCUE. Comparing the results for different lithologies it is interesting to note that some parts of the model are better constrained at depth than closer to ground level. This can be explained by the fact that geological complexity can be more important closer to ground level depending on orientation data, thus increasing uncertainty in such cases. For instance, lithology 3 shows high probability of presence around 2.5 km depth in the bottom left corner of the corresponding plot. Lithology 1 represents the basement, and is defined as the lack of observation of the other units. As such lithology 1 is a proper unit, it embodies the limits of our knowledge where other units are not observed.

Simulating geophysical and petrophysical data

Using the reference geological model, we assigned values of density contrast and magnetic susceptibility to each lithology of section A-B consistently with the structural setting. We assigned a low density contrast and limited magnetic susceptibility to basin fill (lithologies 4, 5 and 6). We assigned higher density contrast and magnetic susceptibilities to lithologies 1, 2 and 3. The petrophysical model, as shown in Figure 5, is directly derived from the reference geological model by assigning values to each lithology (Figure 3). The values we assigned to lithologies have been chosen to obtain contrasts that are close to what could be observed in real scenarios. For density contrast, the background density is set at 2.6 g/cc (or 2600 kg/m^3). This model is used to generate geophysical data for inversion, and is referred to as the reference model.

Magnetic and gravity data were computed at the same horizontal location along the section but at two different altitudes as the aim here is to simulate magnetic airborne (data acquired at 50 m elevation) and gravity ground surveys (data acquired at ground level). Magnetic data are simulated following the same approach as Guo et al. (2015). Gravity data are simulated following Boulanger and Chouteau (2001). We inverted for the horizontal component of the total magnetic field and the vertical component of the Bouguer anomaly assuming a flat topography.

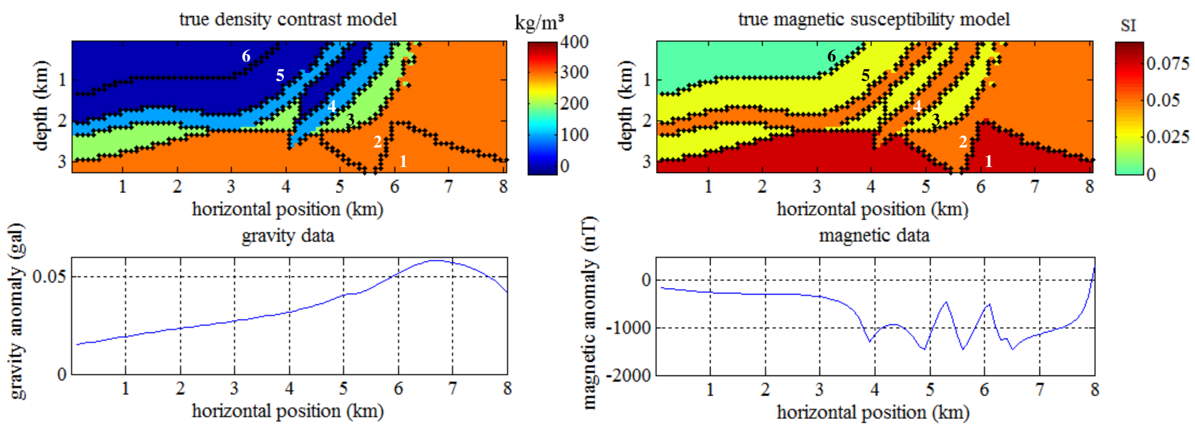

Figure 5. True petrophysical model (top) and simulated geophysical data (bottom). Gravity density contrast (left) is expressed in kg/m³ while magnetic susceptibility has no units. The numbers on the Figure indicate the index assigned to the lithologies as per Figure 3.

In this synthetic dataset we simulated petrophysical measurements using a Gaussian mixture model (GMM). The individual Gaussian distributions making up the simulated petrophysical data have a variance of (40 kg/m³)² for density contrast, (0.01 SI)² for magnetic susceptibility, and a cross-covariance of 0.04 (SI·kg/m³). In this example we describe magnetic susceptibility using Gaussian distributions (although it could also be done using another type of distribution such as lognormal distributions, depending on the petrophysical measurements).

Table 1 – parameters of the mixture model describing petrophysical measurements

Lithology number	Density contrast (kg/m³): cluster	Variance on density contrast ((kg/m³)²)	Magnetic susceptibility (SI): cluster centers (mean)	Variance on magnetic susceptibility	Cross-Covariance (SI·kg/m³)

	centers (mean)				
1	300	1600	0.075	1e-4	0.04
2	300	1600	0.05	1e-4	0.04
3	200	1600	0.025	1e-4	0.04
4	100	1600	0.05	1e-4	0.04
5	0	1600	0.025	1e-4	0.04

Table 1 summarizes the statistical properties of the distributions describing the simulated petrophysical data. The corresponding cross-plot is shown in Figure 6, where the center of the Gaussians correspond to physical property values assigned to the different lithologies of the true model as shown in Figure 3 and Figure 5. In Figure 6, one would notice that the projection of cluster centers on the magnetic susceptibility and density contrast axes overlap. For example, clusters pairs 1, 2 and 5, 6 (2, 4 and 3, 5) have the same center along the density contrast (magnetic susceptibility) axis. In such case, because of this ambiguity, the six geological units cannot be resolved properly without joint interpretation.

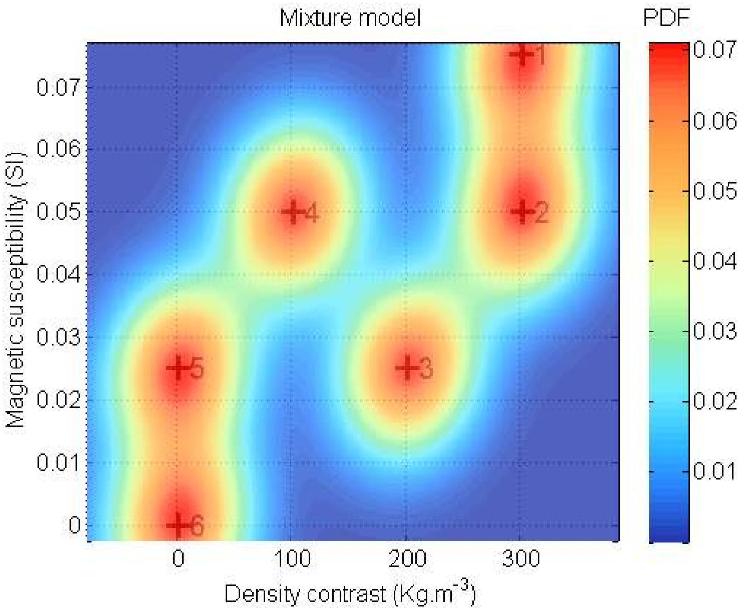

Figure 6. Plot of the mixture model describing petrophysical measurements, as per properties summarized in **Table 1**. The crosses indicate the centre (mean) of the individual distributions making up the mixture model; the associated numbers refer to lithology number as shown on Figure 3.

RESULTS: FROM UNCONSTRAINED SINGLE DOMAIN INVERSION TO CONSTRAINED JOINT INVERISON

Inverted models

We performed a sensitivity analysis to evaluate the influence of prior information and constraints on the inverted model. For single domain inversion we evaluate: unconstrained inversion; inversion with global (e.g., spatially invariant and geologically un-constrained) petrophysical constraints; and inversion with geologically conditioned petrophysical constraints. For joint inversion, we evaluate the use of petrophysical constraints and geologically conditioned petrophysical constraints. The classification of inversion types is summarised in Table 2.

Table 2 – inversion types. The degree of integration increases from (a) to (e). Light blue shading symbolises lower levels of integration while dark blue symbolises higher levels of integration. No shading indicates an absence of integration.

Abbreviation	Inversion attributes	petrophysics	Inversion type	Geology
(a)	No constraints, Single domain inversion	none	Single domain	none
(b)	Single domain inversion, global petrophysical constraints	non-conditioned	Single domain	none
(c)	Joint inversion, global petrophysical constraints	non-conditioned	Joint inversion	none
(d)	Single domain inversion, conditioned petrophysics	conditioned	Single domain	For conditioning and starting model
(e)	Joint inversion, conditioned petrophysics	conditioned	Joint inversion	For conditioning and starting model

The comparison and analysis of results obtained from inversion (a) through (e) (Table 2) constitutes the sensitivity analysis of inversion subject to increasing degrees of integration. It allows us to estimate the contribution of various constraints to inversions and improvements they might bring to the inverted models. The inverted models for inversion (a) through (e) as per Table 2 are shown in Figure 7 for qualitative analysis.

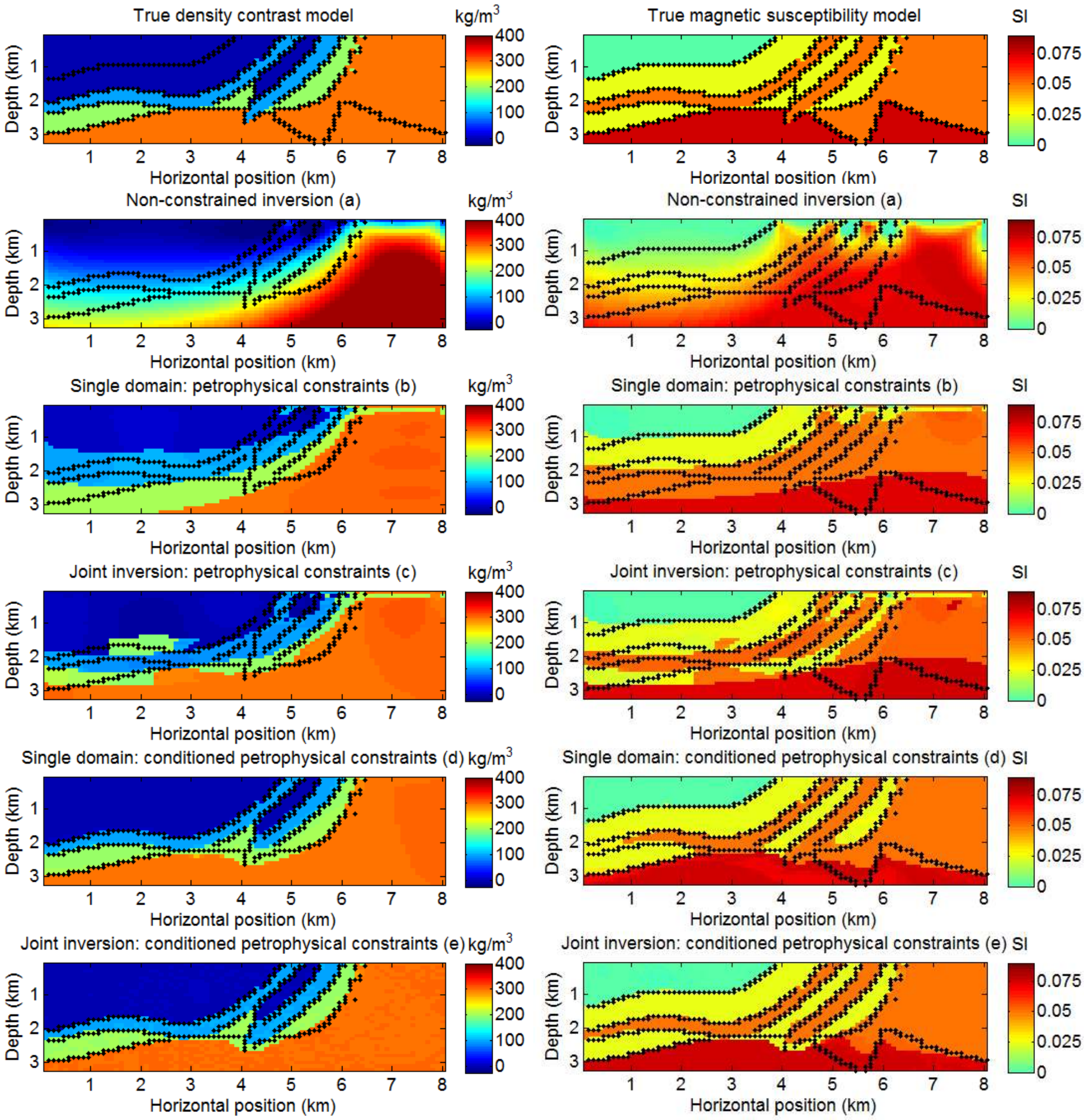

Figure 7. Inversion results for gravity data (left) and magnetics (right). Left column: density contrast, in kg/m³. Right column: magnetic susceptibility. Inversion types are referred to as (a)

through (e) as per Table 2. Black dotted lines represent the interfaces between lithologies in the reference model.

The gravity data (Figure 5) contains long wavelength information, which explains why in this case only the largest structure is resolved by unconstrained gravity inversion (a) (Figure 7a). In contrast, the magnetic data (Figure 5) is able to resolve smaller structures, even though in the case of unconstrained magnetic inversion (a) (Figure 7a) it still only retrieves the largest structures of the model.

From Figure 7, qualitative comparison of inversions (a) through (e) shows that the use of global petrophysical constraints in single domain inversion (Figure 7b) does not resolve the geometry of lithologies accurately. More structural complexity is resolved when petrophysical constraints are applied to joint inversion (Figure 7c), and when petrophysical constraints are conditioned by geological modeling in single domain inversion (Figure 7d). Besides showing models that are consistent with each other, Figure 7e shows improvements in terms of structural geology. Even if noticeable differences occur only at a few locations, unit 1 (basement) is better constrained and unit 4 is better defined and does not link to unit 2 anymore. This improvement is critical because this link could lead to misinterpretation of the basin size.

Results from Figure 7 show that joint inversion allows us to better retrieve complex geometries than single domain inversions, while the use of geologically conditioned petrophysical constraints increases the agreement of retrieved geometries with the reference model. Petrophysical constraints allow us to retrieve values that respect the statistics of surface measurements. As the petrophysical units are well defined in the mixture model matching the statistics of the petrophysical data we simulate, the effect of the constraint is to sharpen the contacts between units. Thus, as can be observed in Figure 7c, petrophysical constraints sharpen the inverted models. As can be seen in Figure 7d geological conditioning makes the inverted model’s geometries closer to that of the reference model. Joint inversions in Figure 7c and Figure 7e increase geological complexity in the inverted model while increasing resemblance to the reference model (when comparing to single domain inversion in Figure 7b and Figure 7d, respectively). Visually, Figure 7e shows results that are closest to the reference model.

Uncertainty Analysis

We analyzed the uncertainty of the results obtained from the different types of inversion in Table 2 and shown in Figure 7 through the calculation of the indicators introduced above. These indicators are the likelihood $\boldsymbol{L}$ (equation 11), the Fisher information $\boldsymbol{I_F}$ (equation 12), and the normalized RMS of the score S_{rms} (equation 14). This assessment allows us to quantify

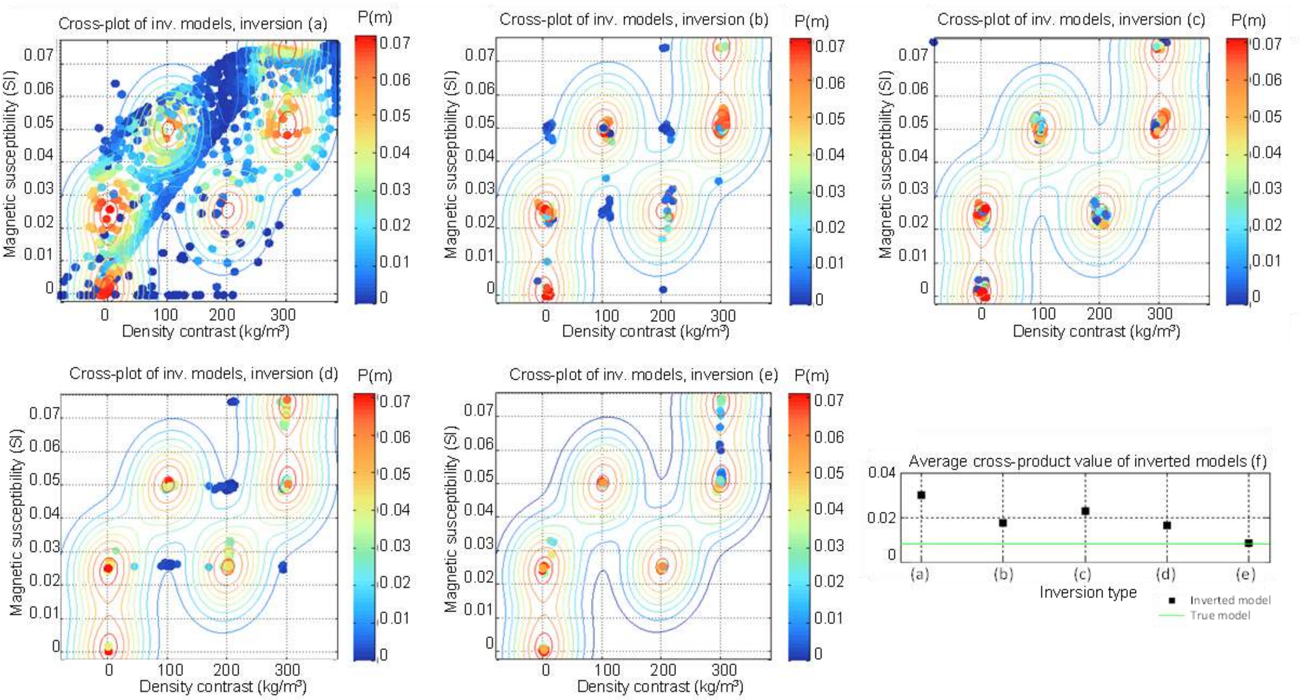

qualitative observations from the inverted models shown in Figure 7. First, we compare the inversion results by displaying the inverted models using cross-plots where inverted physical property values are color-coded by corresponding likelihood values (Figure 8a-e). As an additional indicator, we used the absolute value of the cross-product of the gradients (Figure 8f) to compare the different inversions.

Figure 8. Cross-plots of inverted models for the different levels of integration. Inversion types are referred to as (a) through (e) as per Table 2. The color coding represents likelihood values for each point in the cross-plot. Colored lines are contour levels of the GMM shown in Figure 6. The bottom right plot (f) shows the comparison of cross-product values for different inversions with the true value.

Comparing cross-plots in Figure 8a and in Figure 8b it is observed that petrophysical constraints sharpen the model as inverted data are clustered around specific values. Single domain inversions (Figure 8b) are run separately and the inverted models do not interact: the geometry of inverted models does not match. Therefore, in this case, the ambiguity of cluster centers in single domain inversion is affecting the resulting cross-plot. Results shown in Figure 8b are affected by the ambiguity existing on values of the center of clusters (lower likelihood points shown in blue). On the other hand, to honour the petrophysical constraint in joint inversion (Figure 8c and Figure 8e), inverted values must be clustered around values that belong concurrently to cluster centers along the gravity contrast and magnetic susceptibility axes (higher likelihood points shown in red). Consequently, joint inversion results are less affected by ambiguity.

Ambiguities observed in Figure 8b disappear in Figure 8c as in the latter global petrophysical constraints are applied jointly to the inverted properties. However, ambiguity appears again on Figure 8d when geologically conditioned petrophysical constraints are applied to single domain inversion. Finally, Figure 8e shows that inverting geophysical datasets jointly reduces the remaining ambiguity reduced number of low likelihood). Figure 8f shows the average cross-gradient is, for all 5 inversion types we ran, higher than for the true model. For this indicator , the final product of our workflow (e.g. joint inversion using geologically conditioned petrophysical constraints, inversion (e) as per Table 2) shows values closest to those calculated for the reference model.

In addition to cross-plots with likelihood values, we propose to analyze inversion results using the Fisher information for the inversion types listed in Table 2. Figure 9 shows the relationship between uncertainty and integration degree. It also shows the normalized model RMS error and the normalized RMS value of the score S_{rms}.

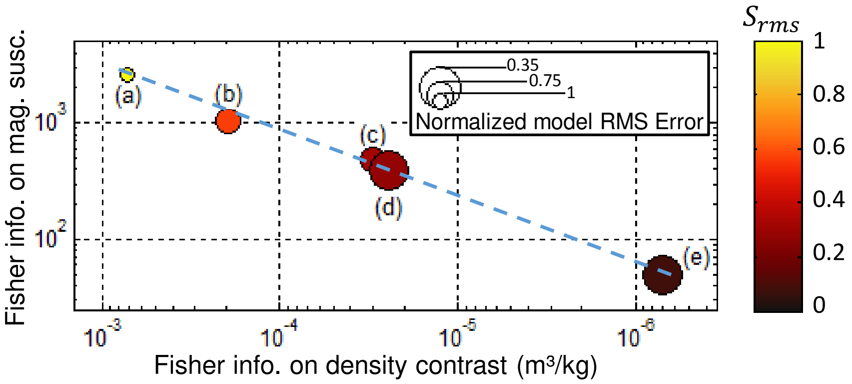

Figure 9. Fisher information for gravity (horizontal axis) and magnetics (vertical axis). Inversion types (a) through (e) are labelled as per Table 2. The dashed blue line represents the linear trend in log-log space that can be observed.

As can be seen in Figure 9, a linear empirical relationship can be derived in log-log space between the Fisher information on magnetic susceptibility and density contrast. The points which lie along the line correspond, from left to right, to increasing levels of integration. This trend being observed in log-log space means that the impact of additional datasets decreases rapidly with the number of datasets already integrated in the inversion scheme.

The Fisher information shows the curvature of the likelihood function around the model, and is therefore an indicator of uncertainty. Consequently, Figure 9 shows that lower levels of integration (inversion (a) and (b)) are strongly affected by non-uniqueness. The resulting likelihood showing higher curvature, the algorithm converged towards a less likely, more uncertain local minimum. This observation is corroborated, to some extent, by both high model RMS misfit and S_{rms} values. Conversely, results obtained from the integration of three different types of data or more (inversions (c), (d) and (e)) show improved Fisher information, lower S_{rms} and model RMS error. Figure 9 shows that, for this synthetic survey, the best results are obtained for inversion (e) (joint inversion with geologically conditioned petrophysical constraints). For inversion (e), the Fisher information has decreased with respect to the least integrated inversions by 3 orders of magnitude for density contrast and by 2 orders of magnitude for magnetic susceptibility. In comparison, calculation of the first term in equation (1) for the different inversions we performed shows that data misfit does not change significantly, and is therefore not shown here. Similarly to other works joint inversion does not decrease data misfit dramatically, and the major improvements occur in model space (Gallardo and Meju, 2004; Abubakar et al., 2012; Johunjuntti and Kamm 2015; Jardani et al., 2012; Gao et al., 2012; Molodstov et al., 2013, Gallardo and Meju, 2011).

Constrained joint inversion with inaccurate starting model

In this subsection we investigate the influence of a starting model that does not accurately incorporate information from geological modeling. Instead of deriving starting models using the result of MCUE combined with petrophysical measurements (equation 10), we use a one-dimensional starting model constituting a vertical positive gradient of density and magnetic susceptibility distributions. The values of the starting model range from 0 g/cc to 3 g/cc and 0 SI to 0.075 SI.

Figure 10 shows the inversion results obtained used for inversion type (e) (Table 2).

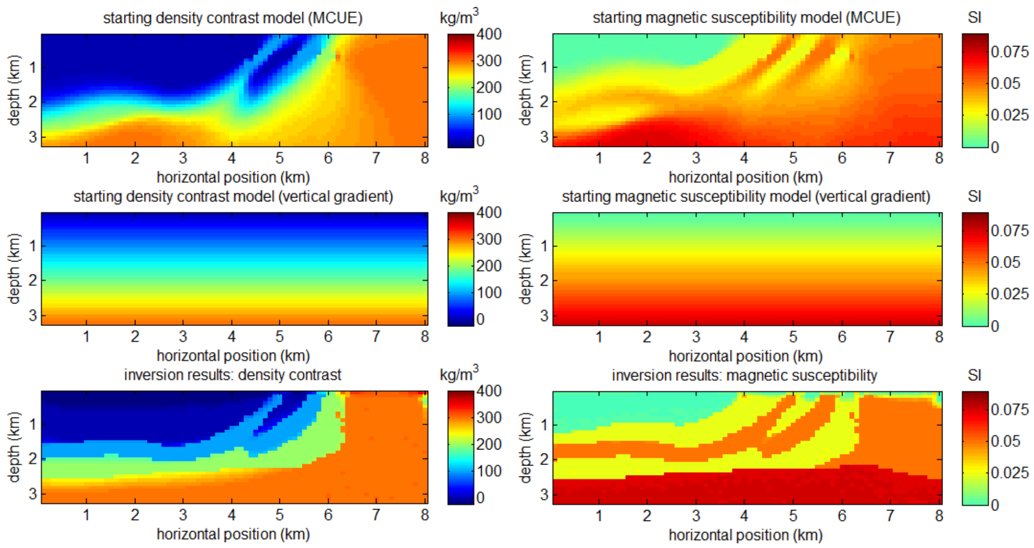

Figure 10. Inverted model obtained through inversion type (e) (bottom row) using a 1D starting model that follows a positive vertical gradient (middle row). For comparison, the starting model derived from MCUE and petrophysical measurements is also shown (first row).

Inversion results shown in Figure 10 show that, except in the deepest, least constrained parts of the model where structural features of the model are guided by the starting model, the inversion methodology is robust to the starting model containing minimum prior information we used. Although the retrieved model lacks the complexity of results shown on Figure 7e, it still retains important features of the geological model. The analysis of quality indicators reveals that the model RMS misfit is in the same order as for inversion (c) (Table 2) and that the values of $\boldsymbol{I_F}$ and S_{rms} are intermediate to inversion (c) and (d).

DISCUSSION

In the examples we showed we assumed that the petrophysics of the models can be described by petrophysical measurements. However, in real case scenarios it is possible that some lithologies have not been sampled by either petrophysics or geology; one approach to mitigating this is to consider this source of uncertainty in the estimation of the mixture model describing petrophysical measurements. We also assumed that the petrophysical measurements show distinct clusters, which is not always the case in nature. When clusters are not easily distinguishable, it is more difficult to differentiate the corresponding geological units through inversion. In such cases, the concerned units might be undistinguishable after conditioning of the petrophysical constraints, thus decreasing the complexity of the geological information contained in the constraints and the influence they may exert on inversion.

We made the arbitrary choice of Gaussian mixtures to describe the petrophysical measurements. Nevertheless, there is no restriction to the type of function used to describe the statistics of these measurements. In the workflow we introduced, the only requirement is for the mixture model to be differentiable, which is the case for almost all the functions that can characterize the statistics of petrophysical measurements.

One of the motivations behind the use of geologically conditioned petrophysical constraints is the incorporation of probabilistic geological information. A less computationally expensive strategy is to estimate the value of an attribute characterizing the medium using geological modeling (for instance MCUE) or expert knowledge to derive less strong constraints for inversion. For example, when using the cross-gradient approach (Gallardo and Meju, 2003), a non-zero objective value reflecting the geology of the area could be used. In the same fashion, when maximizing the correlation between models (Lelièvre et al., 2012) and/or the gradient of the models during joint inversion, an optimum value different from unity can be used to honor prior geological information. In such case, another possibility is to calculate the BP correlation r for the orientation of the gradients in the model. This could be useful in cases similar to the model we used because the cross-product and the correlations we calculate for the true model are different from 0 and 1, respectively (see Figure 8f). In such case, a possible strategy to combine the cross-gradient technique with geological information is to derive local cross-gradient constraints in a fashion similar to the conditioning of petrophysical constraints.

CONCLUSION

We have developed a new inversion workflow that integrates probabilistic geological modeling, petrophysical measurements and geophysical data in a statistical sense. We evaluated the efficacy of the workflow and found it successfully reduces uncertainty. The sensitivity analysis conducted on prior information and inversion constraints shows that inclusion of petrophysical data significantly improves results. Also, the use of geological information from MCUE to condition petrophysical constraints shows better uncertainty and model misfit reduction than when only global petrophysical constraints are applied to inversion, and was particularly effective when used on single-domain constrained inversion. Small differences in the petrophysics of retrieved models and in geophysical data fit between petrophysically conditioned single-domain and joint inversion do not indicate that joint inversion improved results significantly. Nonetheless, from a geological point of view, joint inversion produces results that are more consistent than single-domain inversions. This result is important because decisions made using one or the other of these two models could result in different outcomes (e.g., error in basin size estimation, wrong interpretation of blocking or open fault, etc). In covered terranes, complex regions may be subject to inconsistencies in model construction or be undetectable without surface evidence. In such cases, the use of MCUE in inversion would lead, in portions of the model that depart most from reality, to non-constructed zones where geological structures are difficult to identify. This can reveal the necessity to acquire additional data, to adapt the modelling of these areas, or show the need for targeted exploration.

Some studies focus on one particular aspect of integrated inversion, such as the improvement of a specific joint inversion approach or an original way of using either geological or petrophysical information. More holistic, our approach combines quantitatively, and gives equal importance to petrophysical, geological and geophysical data. Besides providing improved imaging consistent across the different disciplines involved, this workflow allows quantitative evaluation of uncertainty reduction. The adaptability of the described methods permits possible further uncertainty reduction through the integration of additional datasets, adaptation to 3D inversion and implementation on supercomputing platforms for high complexity and resolution datasets. One of the main issues we will have to face is the indirect computation of Hessian matrices by using more sophisticated gradient-based iterative procedures, because direct solvers like Cholesky decomposition are very difficult to scale.

ACKNOWLEDGEMENTS

The authors would like to thank André Revil from the Université de Savoie Mont-Blanc, Chris Wijns from First Quantum Minerals, Peter Lelièvre from the Memorial University of Newfoundland, Eun-Jung Holden from the Centre for Exploration Targeting, University of Western Australia, and Jeffrey Shragge, Colorado School of Mines, and Darren Hunt from Teck Resources Limited for interesting discussions and constructive feedback. We also thank the Geological Survey of Victoria for making the geological data of the Mansfield area publicly available, and Intrepid Geophysics for their support. The authors are also thankful to the Australian Federal government for granting an International Postgraduate Research Scholarship to Jérémie Giraud and the Society of Exploration Geophysicists for granting him the Chevron/SEG Scholarship to provide educational support. The authors acknowledge the State Government of Western Australia for supporting Mark W. Jessell and Mark D. Lindsay through the Geological Survey of Western Australia, Royalties for Regions and the Exploration Incentive Scheme. Mark W. Jessell is supported by a Western Australian Fellowship. The authors also thank Baohai Wu and two other anonymous reviewers for their comments and suggestions during the revision process, which contributed to the improvement of the quality of this paper.

REFERENCES

Abubakar A., G. Gao, T. M. Habashy and J. Liu, 2012, Joint inversion approaches for geophysical electromagnetic and elastic full-waveform data: Inverse Problems, **28**, 1-19, doi:10.1088/0266-5611/28/5/055016.

Alcade, J., C. E. Bond, G. Johnson and R. W. H. Butler, 2017, Impact of image quality on fault interpretation uncertainty: GSA Today, **27**, no. 2, pp. 4-10, doi: 10.1130/GSATG282A.1

Balidemaj E. and R. F. Remis, 2010, A Krylov subspace approach to parametric inversion of electromagnetic data based on residual minimization: PIERS Online, **6**, no. 8, 773-777. doi:10.2529/PIERS091214140937.

Barlow, M. 2004, Density and susceptibility characterization of the minerie 100,000 geology sheet: implication for gravity inversion, July 2004, Y2 PROJECT PMD*CRC, project report: https://d28rz98at9flks.cloudfront.net/67587/67587.pdf

Bennington N. L., H. Zhand, C. H. Thurber and P. A. Bedrosian, 2015, Joint inversion of seismic and magnetotelluric data in the Parkfield Region of California using the normalized cross-gradient constraint: Pure and Applied Geophysics, **172**, p.1033-1052, doi 10.1007/s00024-014-1002-9.

Betts P. G., R. K. Valenta, and J. Finlay, 2003, Evolution of the Mount Woods Inlier, northern Gawler Craton, Southern Australia: an integrated structural and aeromagnetic analysis: Tectonophysics, **366**, 83-111, doi:10.1016/S0040-1951(03)00062-3.

Bond C. E., A. D. Gibbs, Z. K. Shipton and S. Jones, 2007, What do you think this is? "Conceptual uncertainty" in geosciences interpretation: GSA Today, **17**, no. 11, 4-10, doi: 10.1130/GSAT01711A.1.

Bond C. E., G. Johnson and J. F. Ellis, 2015, Structural model creation: the impact of data type and creative space on geological reasoning and interpretation: Special Publication –

Geological Society of London, **421**, 83-87, doi:10.1144/SP421.4.
Bosch M., 1999, Lithologic tomography: from plural geophysical data to lithology estimation: Journal of Geophysical Research, **104**, 749-766, doi: 10.1029/1998JB900014.
Bosch M., 2004, The optimization approach to lithological tomography: Combining seismic and petrophysics for porosity prediction: Geophysics, **69**, no. 5, P.1272-1282, doi: 10.1190/1.1801944.
Bosch M., G. Bertorelli , G. Alvarez, A. Moreno and R. Colmenares, 2015, Reservoir uncertainty description via petrophysical inversion of seismic data: The Leading Edge, **34**, no. 9, 1018-1026, doi: 10.1190/tle34091018.1.
Bosch M., R. Meza, R. Jimenez and A. Hoenig, 2006, Joint gravity and magnetic inversion using 3D Monte Carlo methods: Geophysics, **71**, no. 4, P.G153-156, doi: 10.1190/1.2209952
Bouchedda A., M. Chouteau, A. Bonley B. and B. Giroux, 2012, 2-D joint structural inversion of cross-hole resistance and ground penetrating radar: Journal of Applied Geophysics, **78**, 52-67, doi:10.1088/0266-5611/28/5/055016.
Boulanger O. and M. Chouteau, 2001, Constraints in 3D gravity inversion: Geophysical Prospecting, **49**, 265-280, doi: 10.1046/j.1365-2478.2001.00254.x.
Calcagno P., J. P. Chilès, G. Courrioux, and A. Guillen, 2008, Geological modeling from field data and geological knowledge: Part I. Modeling method coupling 3D potential-field interpolation and geological rules: Physics of the Earth and Planetary Interiors, **171**, no. 1-4, 147-157, doi:10.1016/j.pepi.2008.06.013.
Carter-McAuslan A., P. Lelièvre and C. G. Farquharson, 2015, A study of fuzzy c-means coupling for joint inversion, using seismic tomography and gravity test scenarios: Geophysics, **80**, no. 1, W1-W15, doi: 10.1190/GEO2014-0056.1.
Chen J., M. Hoversten, D. Vasco, R. Rubin and Z. Hou, 2012, A Bayesian model for gas

saturation estimation using marine seismic AVA and CSEM data: Geophysics, **72**, no. 2, P.WA85-WA95, doi: 10.1190/1.2435082.

Colombo D., M. de Stefano, 2007, Geophysical modeling via Simultaneous Joint Inversion of seismic, gravity and electromagnetic data: Application to pre-stack depth imaging: The Leading Edge, **26**, no. 3, pp. 326-331. DOI: 10.1190/1.2715057.

Crooks E., 2015, Discoveries of new oil and gas reserves drop to 20-year low: Financial Times of February 15.

Davis K., D. W. Oldenburg and M. Hillier, 2012, incorporating geologic structures into the inversion of magnetic data: 22nd International Geophysical Conference and Exhibition, Brisbane, Australia.

de la Varga M. and F. Wellmann, 2016, Structural geologic modeling as an inference problem: A Bayesian perspective: Interpretation, **4**, no. 3, SM1-SM16, doi: 10.1190/INT-2015-0188.1.

de Stefano M., F. Golfre Andreasi, S. Re, M. Virgilio and F. F. Snyder, 2011, Multiple-domain, simultaneous joint inversion of geophysical data with application to subsalt imaging: Geophysics, **76**, no. 3, PR69-R80, doi: 10.1190/1.3554652.

Dell'Aversana P., G. Bernasconi, F. Miotti and D. Rovetta, 2011, Joint inversion of rock properties from sonic, resistivity and density well-log measurements: Geophysical Prospecting, **59**, 1144-1154. doi: 10.1111/j.1365-2478.2011.00996.x.

Dell'Aversavna P., G. Bernasconi and F. Chiappa, 2016, A global integration platform optimizing coorperative modeling and simultaneous joint inversion of multi-domain geophysical inversion: AIMS Geosciences, **2**, no. 1, 1-13, doi: 10.3934/geosciences.2016.1.1

Doetsch J., N. Linde, I. Coscia, S. A. Greenhalgh and A. G. Green, 2010, Zonation for 3D aquifer characterization based on joint inversions of multimethod crosshole geophysical data: Geophysics, **75**, no. 6, P.G53-G64, doi: 10.1190/1.3496476.

Fisher R., 1925, Theory of Statistical estimation: Proceedings of the Cambridge Philosophyscal society, **22**, 700-725.

Fregoso E. and L. Gallardo, 2009, Cross-gradients joint 3D inversion with applications to gravity and magnetic data: Geophysics, **74**, no. 4, P.L31-42, doi: 10.1190/1.3119263.

Fullagar P. K., G. A. Pears and B. McMonnies, 2009, Constrained inversion of geologic surfaces – pushing the boundaries: The Leading Edge, **27**, no. 1, 98-105, doi: 10.1190/1.2831686.

Fullagar P. K., G. A. Pears, 2007, Towards Geologically Realistic Inversion, Advances in Geophysical Inversion and Modeling: Paper 28 in Proceedings of Exploration 07: Fifth Decennial International Conference on Mineral Exploration, 446-460. http://www.dmec.ca/ex07-dvd/E07/pdfs/28.pdf

Gallardo L. A., 2007, Multiple cross-gradient joint inversion for geospectral imaging: Geophysical Research Letters, **34**, no. 19, L19301, doi:10.1029/2007GL030409.

Gallardo L. A., S. L. Fontes, M. A. Meju, M. P. Buonora and P. P de Lugao., 2012, Robust geophysical integration through structure-coupled joint inversion and multispectral fusion of seismic reflection, magnetitelluric, magnetic, and gravity images: Example from Santos Basin, offshore Brasil: Geophysics, **77**, no. 5, P.B237-B251, doi: 10.1190/GEO2011-0394.1.

Gallardo L. and M. A. Meju, 2003, Characterization of heterogeneous near-surface materials by joint 2D inversion of dc resistivity and seismic data: Geophysical Research Letters, **30**, no 13, 1-1 – 1-4, doi:10.1029/2003GL017370.

Gallardo L. and M. A. Meju, 2011, Structure-coupled Multiphysics imaging in geophysical sciences: Revue of Geophysics, **49**, no. RG1003, doi:10.1029/2010RG000330.

Gallardo L., M. A. Perez-Flores and E. Gomez-Trevino, 2005, Refinement of three-dimensional multilayer models of basins and crustal environments by inversion of gravity and magnetic data: Tectonophysics, **397**, 37-54, doi:10.1016/j.tecto.2004.10.010.

Gallardo, L. A. and M. A. Meju, 2004, Joint two-dimensional DC resistivity and seismic travel time inversion with cross-gradients constraints: Journal of Geophysical Research, **109**, 3, B03311, doi:10.1029/2003JB002716

Gallardo, L. A. and M. A. Meju, 2009, Structure‐coupled multiphysics imaging in geophysical sciences: Revue of Geophysics, **49**, RG1003, doi:10.1029/2010RG000330

Gao G., A. Abubakar, T. M. Habashy and G. Pan, 2012b, joint petrophysical inversion of electromagnetic and full-waveform seismic data: Geogphysics, **77**, no. 3, PWA3-WA18, doi: 10.1190/GEO2011-0157.1.

Garofalo F., G. Sauvin, L. V. Socco and I. Lecompte, 2015, Joint inversion of seismic and electric data applied to 2D media: Geophysicis, **80**, no. 4, P. EN93-EN104, doi: 10.1190/GEO2014-0313.1.

Giraud J., M. De Stefano and F. Miotti, 2013, Simultaneous joint inversion of electromagnetic and seismic full-waveform inversion – a sensitivity analysis to Biot parameter, extended abstract: 75th EAGE conference and exhibition London ’13, doi: 10.3997/2214-4609.20130797.

Gloaguen E., D. Marcotte. and M. Chouteau, 2004, A new constrained velocity tomography algorithm using geostatistical simulation, extended abstract: tenth international conference on ground penetrating radar, Proceedings of the tenth international conference on ground penetrating radar, 1., IEEE, pp 75–78, doi: 10.1109/ICGPR.2004.179917.Grana D. and E. Della Rossa, 2010, Probabilistic petrophysical-properties estimation integrating statistical rock physics with seismic inversion: Geophysics, **75**, no. 3, O21-O37, doi: 10.1190/1.3386676

Grana D., T. Fjeldstad and H. Omre, 2017, Bayesian Gaussian Mixture Linear Inversion for

Geophysical Inverse Problems: Mathematical Geosciences, pp 1–23, doi:10.1007/s11004-016-9671-9
Guillen A., P. Calcagno, G. Courrioux, A. Joly and P. Ledru, 2008, Geological modeling from field data and geological knowledge Part II. Modeling validation using gravity and magnetic data inversion: Physics of Earth and Planetary Interiors, **171**, no. 1-4, 158-169, doi:10.1016/j.pepi.2008.06.014.
Guo Z.-Y, D.-J. Liu, Q. Pan, and Y.-Y. Zhang, 2015, Forward modeling of total magnetic anomaly over a pseudo-2D underground ferromagnetic pipeline: Journal of applied geophysics, **113**, 14-30. doi:10.1088/1742-2132/12/3/340.
Gyulai A., M. K. Baracza and E. E. Tolnai, 2013, The application of joint inversion in geophysical exploration: International Journal of Geosciences 2013, **4**, 283-289, doi: 10.4236/ijg.2013.42026.
Haber E., and Oldenburg D., 1996, Joint inversion: structural approach: Inverse Problems, **13**, 63-77. PII, doi: S0266-5611(97)74070-X.
Hastie T., R. Tibshirani and J. Friedman, 2009, The Elements of Statistical Learning Data Mining, Inference, and Prediction, 2009, Second Edition: Springer Series in statistics, Springer.
Hatfield K. L., A. J. Evans and P. K. Harvey, 2002, Defining petrophysical units of the Palmer Deep sites from let 178: Proceedings of the Ocean Drilling Program, Scientific Results. Ocean Drilling Program, pp1-pp17.
Hillier M. J., E. M. Schetselaar, E. A. de Kemp and G. Perron, 2014, Three-dimensional modeling of geological surfaces using generalized interpolation with radial basis functions: Mathematical Geosciences, **46**, no. 8, pp. 931-953, doi: 10.1007/s11004-014-9540-3.
Hoversten G. M., F. Cassassuce, E. Gasperikova, G. A. Newman, J. Chen, Y. Rubin, Z. Hou

and D. Vasco, 2006, Direct reservoir parameter estimation using joint inversion of marine seismic AVA and CSEM data: Geophysics, **71**, no. 3, C1-C13, doi: 10.1190/1.2194510.

Hu W., A. Abubakar and T. M. Habashy, 2009, Joint electromagnetic and seismic inversion using structural constraints: Geophysics, **74**, no. 6, P.R99-109, doi: 10.1190/1.3246586.

Jardani A., A. Revil and J. P. Dupont, 2013, Stochastic joint inversion of hydrogeophysical data for salt tracer test monitoring and hydraulic conductivity imaging: Advances in Water Resources, **52**, 62-77, doi: 10.1016/j.advwatres.2012.08.005.

Jessell M. W. and R. K. Valenta, 1996, Structural geophysics: Integrated structural and geophysical modeling, *in* Declan: Computer Methods in the Geosciences, **15**, 303-324, doi: 10.1016/S1874-561X(96)80027-7.

Jessell M. W., L. Aillères and E. A. de Kemp, 2010, Towards an integrated inversion of geoscientific data: What price of geology?: Tectonophysics, **490**, 294-306. doi:10.1016/j.tecto.2010.05.020.

Jessell M. W., L. Aillères and E. A. de Kemp, M. Lindsay, F. Wellmann, M. Hillier, G. Laurent, T. Chamichael and R. Martin, 2014, Next generation three-dimensional geological modeling and inversion, from Society of Economic Geologists, Special Publication, **18**, pp. 261-272.

Jessell M. W., L. Aillères and E. A. de Kemp, M. Lindsay, F. Wellmann, M. Hillier, G. Laurent, T. Chamichael and R. Martin, 2015, Geological uncertainty and geophysical inversion: 24^{th} International Geophysical Conference and Exhibition, ASEG, Expanded Abstract, doi: 10.1071/ASEG2015ab108.

Juhojuntti N. and J. Kamm, 2015, Joint inversion of seismic refraction and resistivity data using layered models – applications to groundwater investigation: Geophysics, **80**, no. 1, P.EN43-EN55, doi: 10.1190/GEO2013-0476.1.

Kitanidis P. K., 1995, Quasi-linear geostatistical theory for inversing: Water Resources

Research, **31**, no. 10, 2411-2419, doi: 10.1029/95WR01945

Lane R. and A. Guillen, 2005, Geologically-inspired constraints for a potential field litho-inversion scheme: Proceedings of IAMG'05: GIS and Spatial Analysis, **1**, 181-186.

Lane R., P. McInerney and R. Seikel, 2009, Using a 3D geological mapping framework to integrate AEM, gravity and magnetic modelling - San Nicolas case history: 20th ASEG International Geophysical Conference and Exhibition, ASEG, Expanded Abstract, doi: http://dx.doi.org/10.1071/ASEG2009ab043.

Lelièvre P. G. and D. W. Oldenburg, 2009, A comprehensive study of including structural orientation information in geophysical inversions: Geophysical Journal International, **178**, no. 2, 623-637.

Lelièvre P. G, C. Farquharson C. A. Hurich, 2012, Joint inversion of seismic traveltimes and gravity data on unstructured grids with application to mineral exploration: Geophysics, **77**, no. 1, P.K1-K15, doi: 10.1190/GEO2011-0154.1.

Li M., A. Abubakar, T. M. Habashy and Y. Zhang, 2010, Inversion of controlled-source electromagnetic data using a model-based approach: Geophysical Prospecting, **58**, 455-467, doi: 10.1111/j.1365-2478.2009.0824.x.

Lelièvre P. G., C. Farquharson and Bijani R., 2015, 3D stochastic geophysical inversion for contact surface geometry: Geophysical Research Abstract 17 EGU201503627, European Geophysical Union General Assembly 2015, EGU, Abstract.

Li Y. and D.W. Oldenburg, 1996, 3D inversion of magnetic data: Geophysics, **61**, no. 2, 394-408, doi: DOI: 10.1190/1.1443968.

Li Y. and D.W. Oldenburg, 1998, 3D inversion of gravity data: Geophysics, **63**, no. 1, 109–119, doi: DOI: 10.1190/1.1444302.

Li, X. and M. Chouteau, 1998, Three-Dimensional Gravity Modeling In All Space: Surveys in Geophysics, **19**, no. 4, 339-368, doi:10.1023/A:1006554408567

Liang L., A. Abubakar and T. M. Habashy, 2016, Reservoir property mapping and monitoring from joint inversion of time-lapse seismic, electromagnetic, and production data: Geophysics, **81**, no. 5, P. ID73–ID84, doi: 10.1190/GEO2015-0620.1

Linde N., Binley A., A. Tryggvason, L. B. Pedersen and A. Revil, 2006, Improved hydrogeophysical characterization using joint inversion of cross-hole electrical resistance and ground-penetrating radar traveltime data: Water Resources Research, **42**, W12404, doi:10.1029/2006WR005131.

Lindsay M. D., M. W. Jessell, L. Aillères, S. Perrouty, E. A. de Kemp and P. G. Betts, 2013b, Geodiversity: Exploration of 3D geological model space: Tectonophysics, **594**, 27-37, doi: 10.1016/j.tecto.2013.03.013.

Lindsay M. D., S. Perrouty, M. W. Jessell and L. Aillères, 2013a, Making the link between geological and geophysical uncertainty: geodiversity in the Ashanti Greenstone Belt: Geophysical Journal International, **195**, 903-922, doi: 10.1093/gji/ggt311.

Lindsay M. D., S. Perrouty, M. W. Jessell and L. Aillères, 2014, Inversion and geodiverity: searching model space for the answers: Mathematical Geosciences, **46**, 971-1010, doi: 10.1007/s11004-014-9538-x.

Mahardika H., A. Revil and A. Jardani, 2012, Waveform joint inversion of seismograms and electrograms for moment tensor characterization of fracking events: Geophysics, **77**, no. 5, P.ID23-ID39, doi: 10.1190/GEO2012-0019.1.

Mantovani M. S. M., V. H. A. Louro, V. B. Ribeiro, H. S. Requejo and R. P. Z. dos Santos, 2016, Geophysical analysis of Catalao I alkaline-carbonatite complex in Gioas, Brazil: Geophysical Prospecting, **64**, 216-227, doi: 10.1111/1365-2478.12283.

Martin R., V. Monteiller, D. Komatitsch, S. Perrouty, M. Jessell, S. Bonvalot and M. Lindsay, 2013, Gravity inversion using wavelet-based compression on parallel hybrid CPU/GPU systems: application to southwest Ghana: Geophysical Journal International, **195**, no. 3, 1594-1619, doi: 10.1093/gji/ggt334.

Martinez C., Y. Li, R. Krahenbuhl, M. A. Braga, 2012, Structurally constrained lithology characterization using magnetic and gravity gradient data over an iron ore formation: 22nd International Geophysical Conference and Exhibition, ASEG, Expanded Abstract, doi: 10.1071/ASEG2012ab211.

McCalman L., S. T. O'Callaghan, A. Reid, D. Shen, S. Carter, L. Krieger, G. Beardsmore, E. V. Bonilla and F. T. Ramos, 2014, Distributed Bayesian geophysical inversions: Proceedings of the thirty-ninth workshop on geothermal reservoir engineering, Stanford University, California, February 24-26.

McMillan M. S., D. W. Oldenburg, E. Haber and C. Scharzbach, 2015, Parametric 3D inversion of airborne time domain electromagnetics: 24th International Geophysical Conference and Exhibition,ASEG, Expanded Abstract, doi: 10.1071/ASEG2015ab101

Medina E., F. Miotti, S. Ratti, S. Sangewar, D. L. Andreis and J. Giraud 2015, Seismic and electromagnetic integration through petrophysical joint inversion workflow for prospect characterization: SEG International Exposition and 85th Annual Meeting, SEG, Expanded Abstracts, 844 – p.848, doi: 10.1190/segam2015-5878252.1.

Miotti F. and J. Giraud, 2015, Joint inversion of attributes: US Patent 20,150,362,623. https://patents.google.com/patent/US20150362623A1/en.

Miotti F., I. Guerra, A. Lovatini, M. Paydayesh, M. Leathard and G. Kramer, 2015, Estimation of petrophysical model via joint inversion of seismic and EM datasets: 25th international geophysical conference and exhibition Perth 2015 ASEG, Expanded Abstract, doi: 10.1071/ASEG2015ab158.

Molodtsov D. M., V. N. Troyan, Y. V. Roslov and A. Zerilli, 2013, Joint inversion of seismic traveltimes and magnetotelluric data with a directed structural constraint: Geophysical prospecting, **61**, 1218-1228, doi: 10.1111/1365-2478.12060

Moorkamp M., B. Heincke, M. Jegen, A. W. Roberts and R. W. Hobbs, 2011, A framework for 3-D joint inversion of MT, gravity and seismic refraction data: Geophysical Journal International, **184**, 477-493, doi: 10.1111/j.1365-246X.2010.04856.x.

Moorkamp M., P. Lelièvre , N. Linde, A. Khan, 2016, Integrated Imaging of the Earth: Theory and Applications: American Geophysical Union, John Whiley & Sons ISBN: 978-1-118-92905-6, 270 pages. .

Moorkamp, M., A. W. Roberts, M. Jegen, B. Heincke,and R. W. Hobbs, 2013, Verification of velocity-resistivity relationships derived from structural joint inversion with borehole data: Geophysical Research Letters, **40**, 3596–3601, doi:10.1002/grl.50696

Paasche H. and J. Tronicke, 2007, Cooperative inversion of 2D geophysical data sets: A zonal approach based on fuzzy c-means cluster analysis: Geophysics, **72**, no. 3, A35-A39, doi: 10.1190/1.2670341

Pakyuz-Charrier E., M. D. Lindsay and M. W. Jessell, 2015, Geological models need error bars! Handling uncertainty in 3D geological modelling: Saying Goodbye to a 2D earth conference, Margaret River (Werstern Australia), Abstract, Conference organized by the Centre for Exploration Targeting, University of Western Australia.

Rao N. V. C., 2008, Petrophysical properties of Indian Kimberlintes, Lamproites and Lamprophyres, *in* INDIAN DYKES: Geochemistry, Geophysics and Geochronology, Editors: Srivastava R. K., Sivaj C. and Rao N. V. C, Narosa Publishing House Pvt, New Dehli, India.

Rapstine T., Y. Li, and J. Sun, 2016, Integrating a spatial salt likelihood map and prior petrophysical data into a gravity gradiometry inversion through fuzzy c-means clustering: International Exposition and 86th Annual Meeting, SEG, Expanded Abstract, pp. 1622-1626, doi: 10.1190/segam2016-13949789.1

Reid A., S. T. O'Callaghan, E. V. Bonilla, L. McCalman, T. Rawling and F. Ramos, 2013, Bayesian Joint Inversions for the Exploration of Earth Resources: Proceedings of the twenty-third international joint conference on artificial intelligence, P.2877-2884, doi: 10.1.1.415.9471.

Revil A., S. Cuttler, M. Karaoulis, J. Zhou, B. Raynolsd and M. Batzle, 2015, The plumbing system of the Pagosa thermal Springs, Colorado: Application of geologically constrained geophysical inversion and data fusion: Journal of Volcanology and Geothermal Research, **299**, 1–18, doi: http://dx.doi.org/10.1016/j.jvolgeores.2015.04.005

Roberts A. W., R. W. Hobbs, M. Goldstein, M. Moorkamp, M. Jegen and H. Bjoern, 2016, Joint Stochastic constraint of a large data set from a salt dome: Geophysics, **81**, no. 2, P.ID1-ID24, doi: 10.1190/GEO2015-0127.1 .

Rubin Y., G. M. Hoversten, Z. Hou and J. Chen, 2006, risk reduction in gas reservoir exploration using joint seismic-EM inversion, Gas Tips, Winter 2006, 5-9, http://www.ce.berkeley.edu/sites/default/files/assets/users/rubin/GasTIPS-Berkeley.pdf

Schodde R. C., 2010, Global discovery trends 1950-2009: What, where and who found them: presented at PDAC Toronto on 7 March 2010.

Schodde R. C., 2014, Challenges and opportunities for under-cover exploration in Australia: Presentation to the UNCOVER Summit 2014, Adelaide, March 2014.

Scholl C., J. Neumann, M. D. Watts, S. Hallinan and S. Mulè, 2016, Geologically constrained 2D and 3D airborne EM inversion through cross-gradient regularization and multi-grid efficiency: 25th Geophysical Conference and Exhibition, ASEG, Expanded Abstract, doi: http://dx.doi.org/10.1071/ASEG2016ab229

Shamsipour P., D. Marcotte and M. Chouteau, 2012, 3D stochastic joint inversion of gravity and magnetic data: Journal of applied geophysics, **79**, 27-37, doi:10.1016/j.jappgeo.2011.12.012.

Snodgrass M. F. and P. K. Kitanidis, 1997, A geostatistical approach of contaminant source identification: Water Resources Research, **33**, no. 4, 537-546, doi: 10.1029/96WR03753

Sun J. and Y. Li, 2012, Joint inversion of multiple geophysical data: A petrophysical approach using guided fuzzy c-means clustering: SEG 82nd Annual Meeting, SEG, Extended Abstract, doi: 10.1190/segam2012-1388.1.

Sun J. and Y. Li, 2013, A general framework for joint inversion with petrophysical information as constraints: SEG 83rd Annual Meeting , SEG, Expanded Abstract, pp. 3093-3097, doi: 10.1190/segam2013-1185.1

Sun J. and Y. Li, 2015, Multidomain petrophysically constrainted inversion and geology differentiation using guided fuzzy c-means clustering: Geophysicis, **80**, no. 4, P. ID1-ID18, doi: 10.1190/GEO2014-0049.1.

Sun J. and Y. Li, 2016, Joint inversion of multiple geophysical and petrophysical data using generalized fuzzy clustering algorithms: Geophysical Journal International, **208**, 1201–1216, doi: 10.1093/gji/ggw442

Sun J. and Y. Li, 2016, Joint inversion of multiple geophysical data using guided fuzzy c-means clustering: Geophysics, **81**, no. 3, P.ID37-ID57, doi: 10.1190/GEO2015-0457.1.

Tarantola A., 1984, Inversion of seismic reflection data in the acoustic approximation: Geophysics, **49**, no. 8, 1259-1266. doi: 10.1190/1.1441754

Tarantola A., 2005, Inverse problem theory and Methods for data fitting and model parameter estimation: Society of Industrial and Applied Mathematics Philadelphia, PA.

Tschirhart V., C. W. Jefferson and W. A. Morris, 2016, Basement geology beneath the northeast Thelon Basin, Nunavut: insights from integrating new gravity, magnetic and geological data: Geophysical Prospecting (Version of Record online: 8 AUG 2016), doi: 10.1111/1365-2478.12430.

Vozoff K. and D. L. B. Jupp, 1975, Joint inversion of geophysical data: Geophysical Journal of the Royal Astronomical Society, **42**, 977-991, doi: 10.1111/j.1365-246X.1975.tb06462.x.

Wellmann J. F. and K. Regenauer-Lieb, 2012, Uncertainties have a meaning: information entropy as a quality measure for 3-D geological models: Tectonophysics, **526**, p. 207-216, doi: 10.1016/j.tecto.2011.05.001.

Wellmann J. F., S. Finsterle, A. Croucher, 2013, Integrating structural geological data into the inverse modeling framework of iTOUCH2: Computers & Geosciences, **65**, 95-109, doi: 10.1016/j.cageo.2013.10.014.

Williams N. C., 2009, Mass and magnetic properties for 3D geological and geophysical modeling of the southern Agnew–Wiluna Greenstone Belt and Leinster nickel deposits, Western Australia: Australian Journal of Earth Sciences, **56**, p. 1111-1142, doi: 10.1080/08120090903246220.

Zhang J. and A. Revil, 2015, 2D joint inversion of geophysical data using petrophysical clustering and facies deformation: Geophysics, **80**, no. 5, M69-M88, doi: 10.1190/GEO2015-0147.1.

Zhou J., A. Revil and A. Jardani, 2016, Stochasic structure-constrained image-guided inversion of geophysical data: Geophysics, **81**, no. 2, E89-E101, doi: 10.1190/GEO2014-0569.1.

Figures and Tables

Figure 1. Integrated joint inversion workflow summary illustrating the interaction between geology, petrophysics and geophysics. 9

Figure 2. Principle of conditioning of petrophysical constraints by EG. 16

Figure 3. Reference geological model used for geological modeling. Faults are shown by black lines in map view. The left part shows the map view while the right hand part shows the extracted cross-section A-B, which has been extracted from this volume and is used as the reference geological model. The numbers on the Figure indicate the index assigned to the lithologies. 20

Figure 4. Probability of presence for the different lithologies for cross-section A-B. These probabilities have been obtained from MCUE on the whole geological model and extracted along the cross-section to be used in a 2D setting. 21

Figure 5. True petrophysical model (top) and simulated geophysical data (bottom). Gravity density contrast (left) is expressed in kg/m³ while magnetic susceptibility has no units. The numbers on the Figure indicate the index assigned to the lithologies as per Figure 5. 23

Figure 6. Plot of the mixture model describing petrophysical measurements, as per properties summarized in Table 1. The crosses indicate the centre (mean) of the individual distributions making up the mixture model; the associated numbers refer to lithology number as shown on Figure 3. 25

Figure 7. Inversion results for gravity data (left) and magnetics (right). Left column: density contrast, in kg/m³. Right column: magnetic susceptibility. Inversion types are referred to as (a) through (e) as per Table 2. Black dotted lines represent the interfaces between lithologies in the reference model... 27

Figure 8. Cross-plots of inverted models for the different levels of integration. Inversion types are referred to as (a) through (e) as per Table 2. The color coding represents likelihood values for each point in the cross-plot. Colored lines are contour levels of the GMM shown in Figure 6. The bottom right plot (f) shows the comparison of cross-product values for different inversions with the true value. 30

Figure 9. Fisher information for gravity (horizontal axis) and magnetics (vertical axis). Inversion types (a) through (e) are labelled as per Table 2. The dashed blue line represents the linear trend in log-log space that can be observed. 31

Figure 10. Inverted model obtained through inversion type (e) (bottom row) using a 1D starting model that follows a positive vertical gradient (middle row). For comparison, the starting model derived from MCUE and petrophysical measurements is also shown (first row). 33

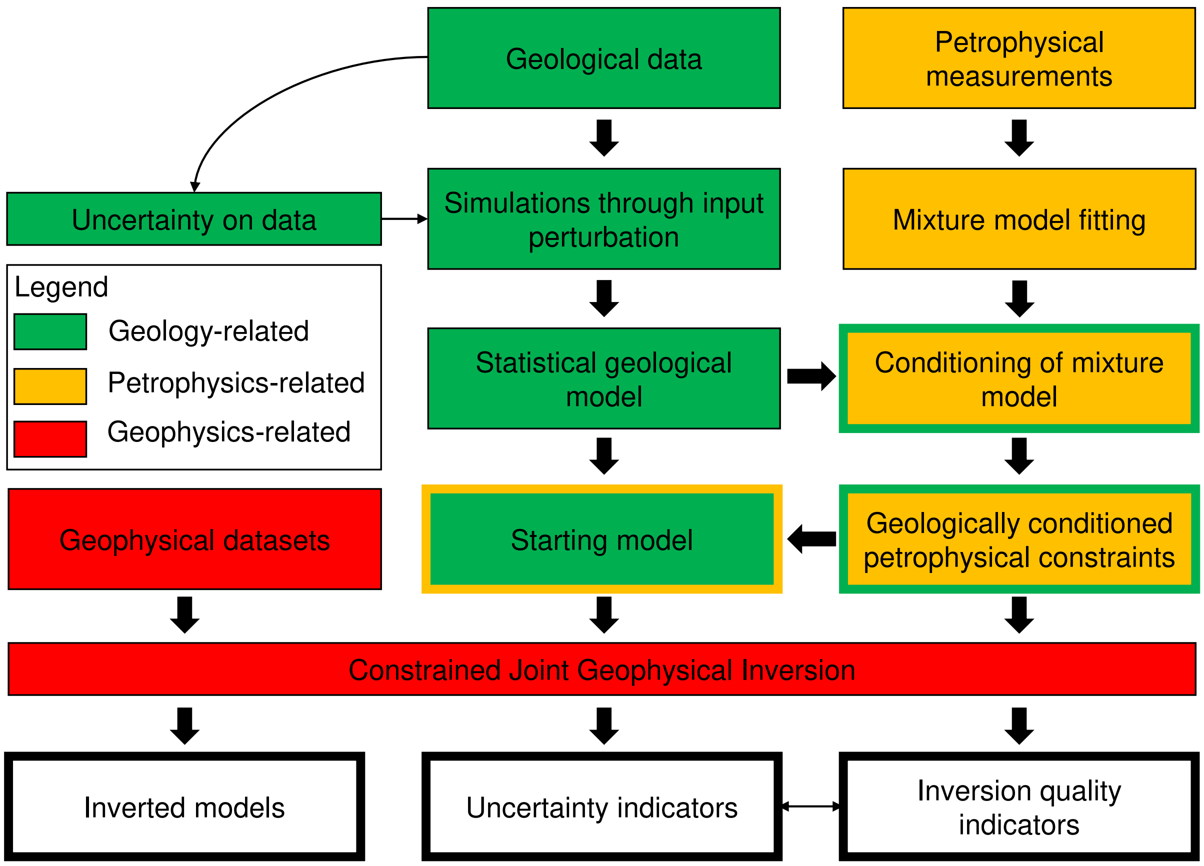

Figure 11. Integrated joint inversion workflow summary illustrating the interaction between geology, petrophysics and geophysics.

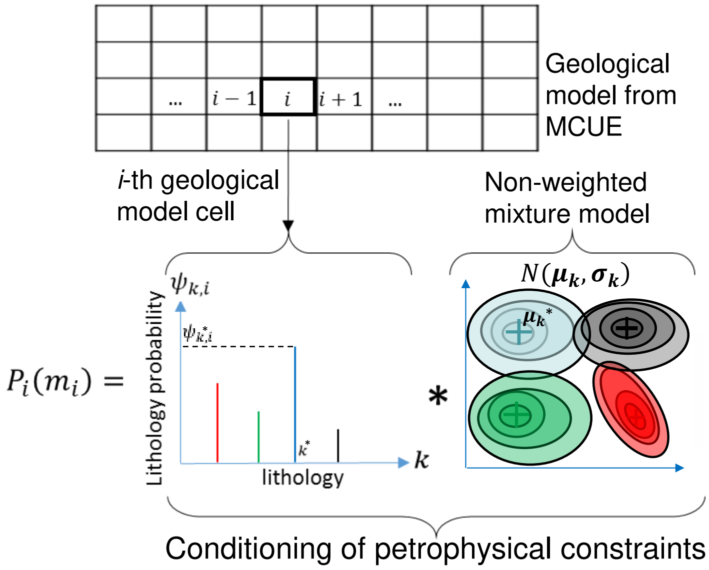

Figure 12. Principle of conditioning of petrophysical constraints by EG.

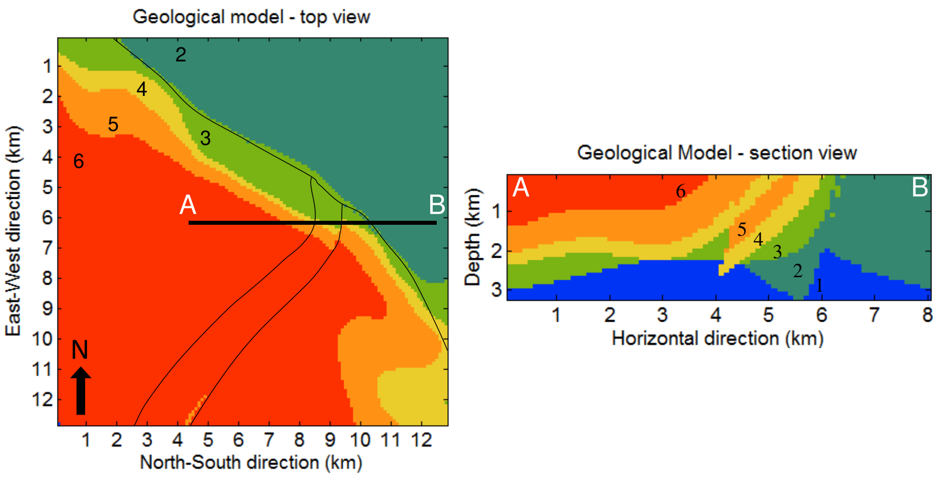

Figure 13. Reference geological model used for geological modeling. Faults are shown by black lines in map view. The left part shows the map view while the right hand part shows the extracted cross-section A-B, which has been extracted from this volume and is used as the reference geological model. The numbers on the Figure indicate the index assigned to the lithologies.

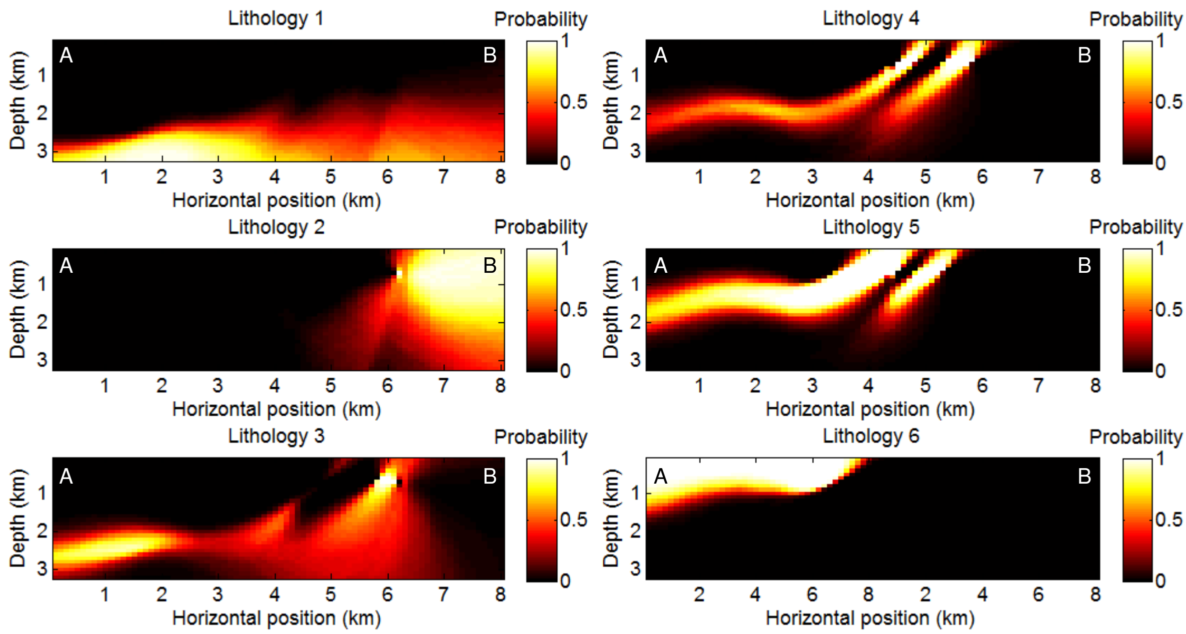

Figure 14. Probability of presence for the different lithologies for cross-section A-B. These probabilities have been obtained from MCUE on the whole geological model and extracted along the cross-section to be used in a 2D setting.

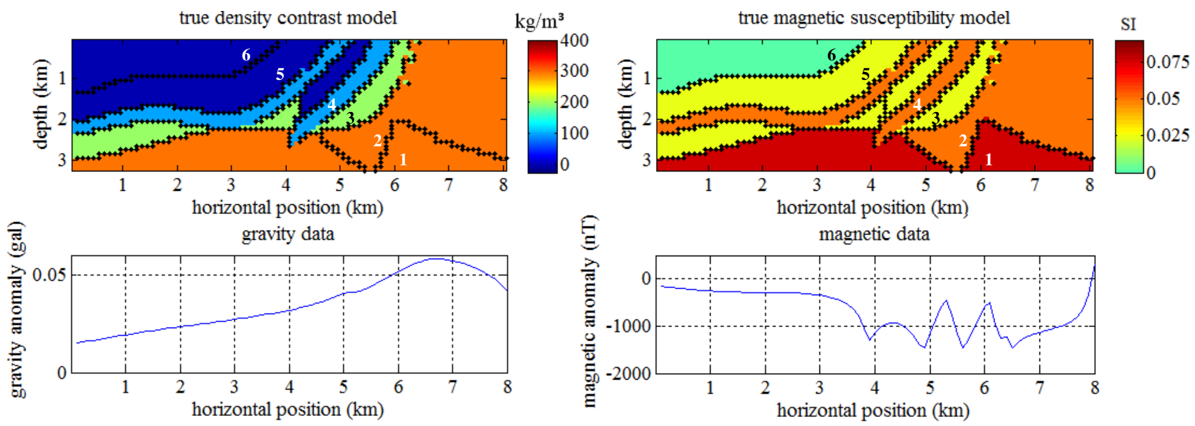

Figure 15. True petrophysical model (top) and simulated geophysical data (bottom). Gravity density contrast (left) is expressed in kg/m³ while magnetic susceptibility has no units. The numbers on the Figure indicate the index assigned to the lithologies as per Figure 3.

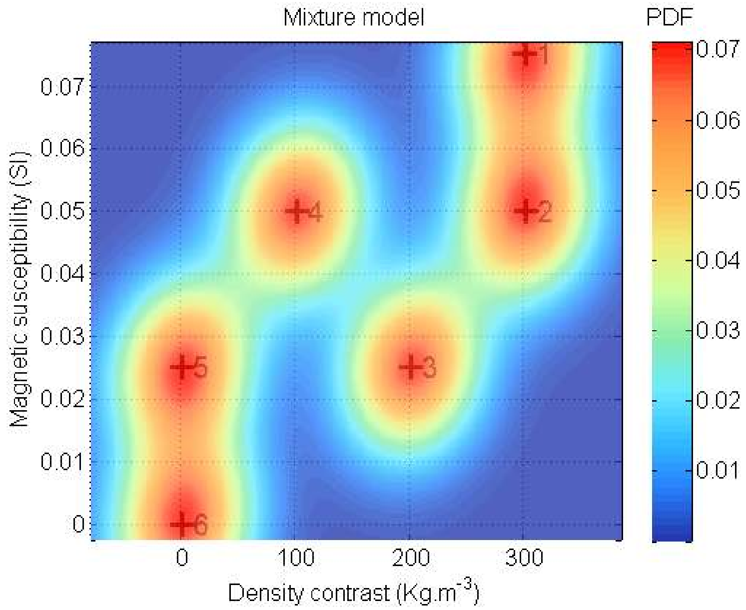

Figure 16. Plot of the mixture model describing petrophysical measurements, as per properties summarized in **Table 1**. The crosses indicate the centre (mean) of the individual distributions making up the mixture model; the associated numbers refer to lithology number as shown on Figure 3.

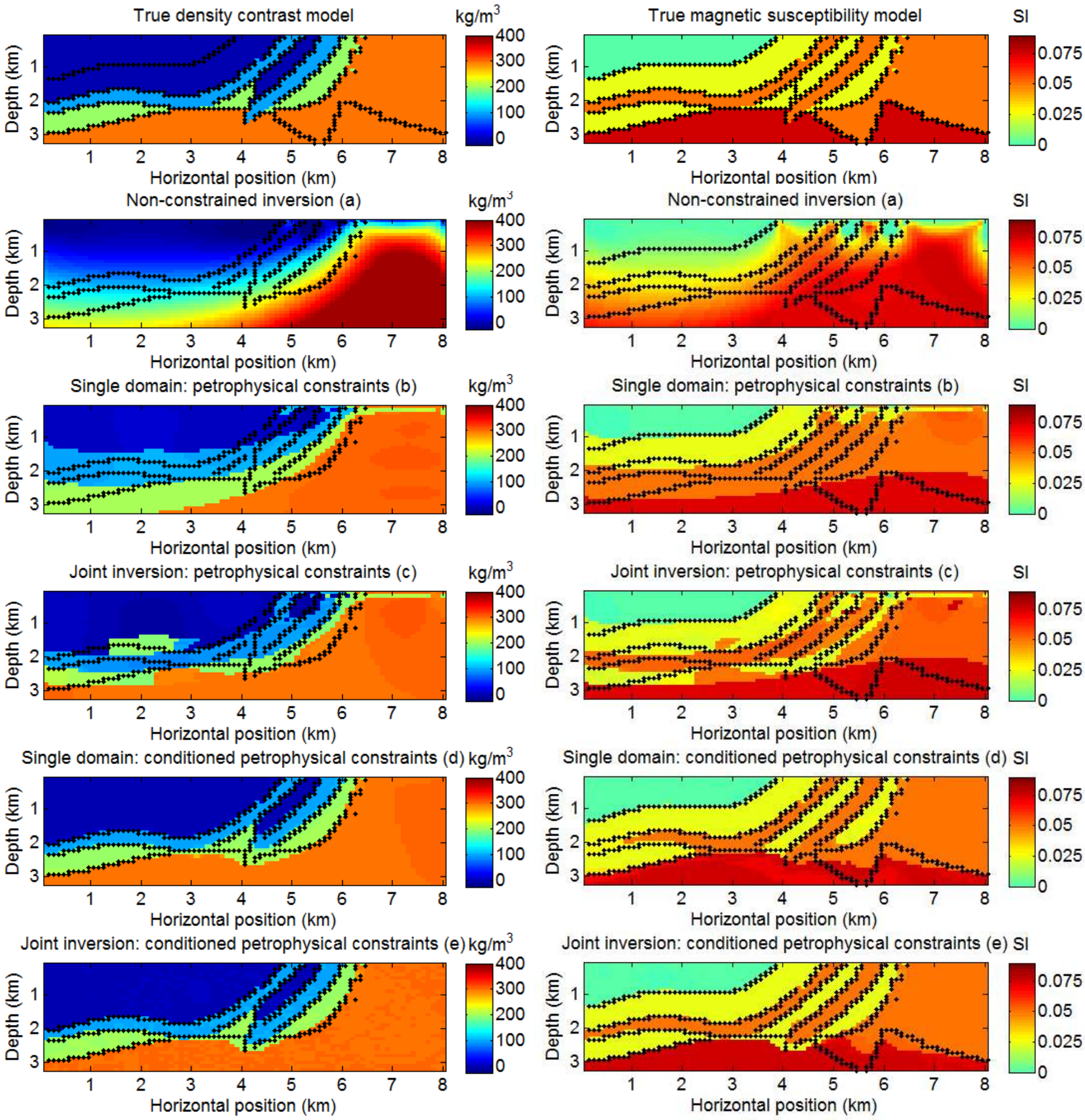

Figure 17. Inversion results for gravity data (left) and magnetics (right). Left column: density contrast, in kg/m³. Right column: magnetic susceptibility. Inversion types are referred to as (a) through (e) as per Table 2. Black dotted lines represent the interfaces between lithologies in the reference model.

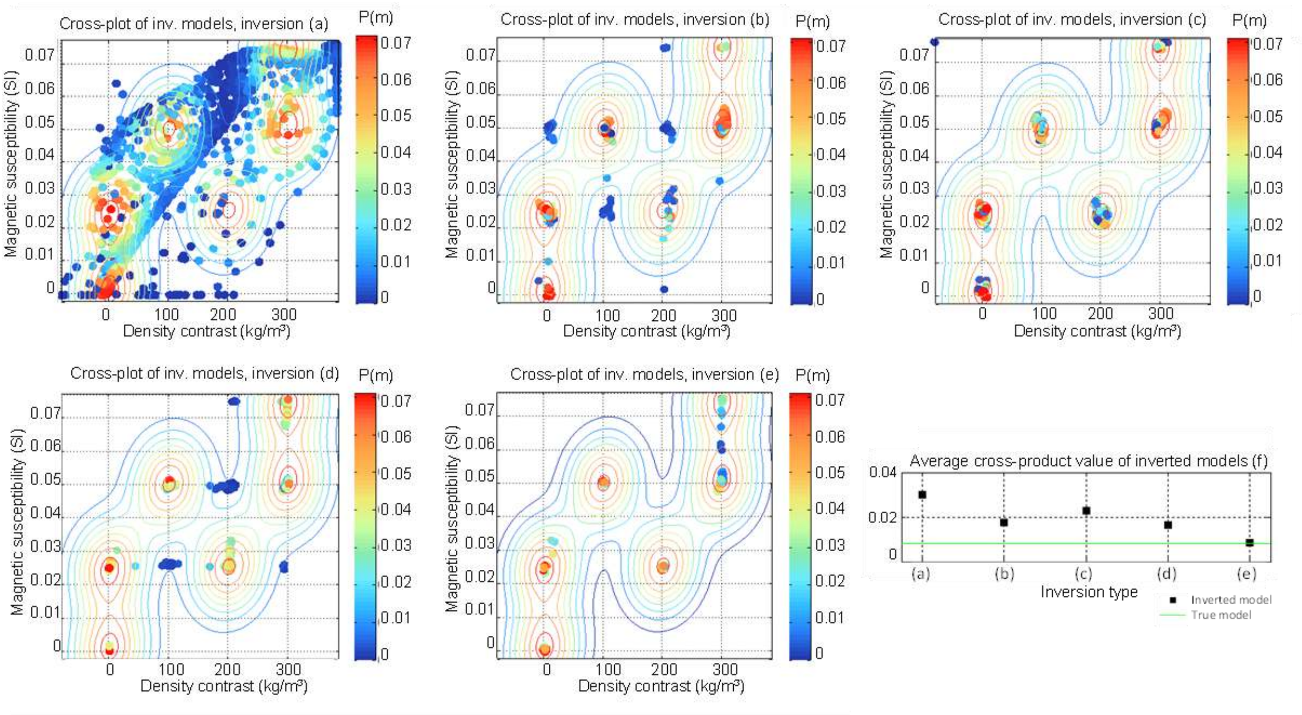

Figure 18. Cross-plots of inverted models for the different levels of integration. Inversion types are referred to as (a) through (e) as per Table 2. The color coding represents likelihood values for each point in the cross-plot. Colored lines are contour levels of the GMM shown in Figure 6. The bottom right plot (f) shows the comparison of cross-product values for different inversions with the true value.

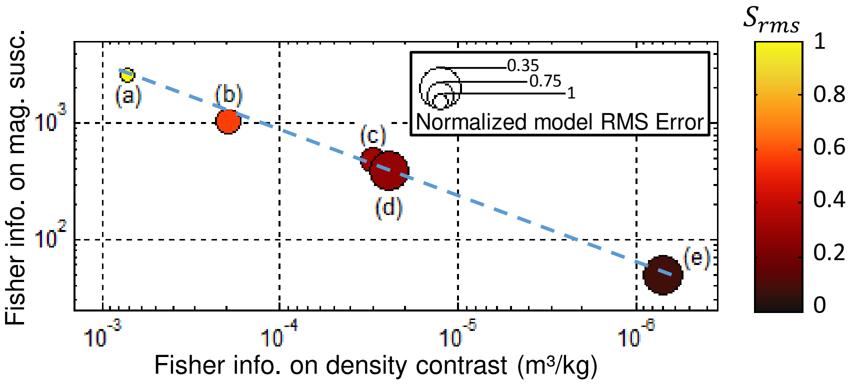

Figure 19. Fisher information for gravity (horizontal axis) and magnetics (vertical axis). Inversion types (a) through (e) are labelled as per Table 2. The dashed blue line represents the linear trend in log-log space that can be observed.

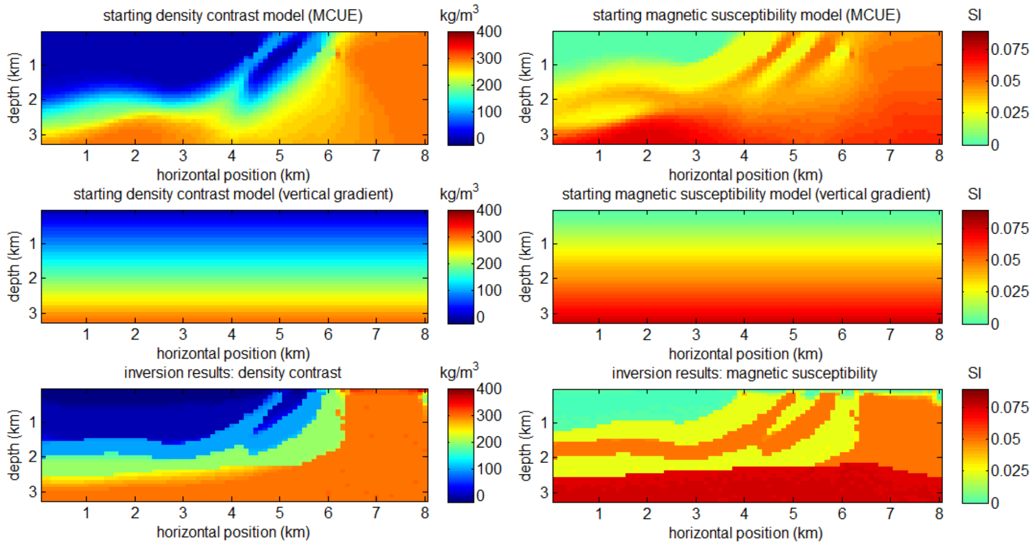

Figure 20. Inverted model obtained through inversion type (e) (bottom row) using a 1D starting model that follows a positive vertical gradient (middle row). For comparison, the starting model derived from MCUE and petrophysical measurements is also shown (first row).